

## Regimes of cavity QED under incoherent excitation: From weak to deep strong coupling

Alberto Mercurio,<sup>1,\*†</sup> Vincenzo Macrì<sup>2,\*‡</sup>, Chris Gustin,<sup>3,4</sup> Stephen Hughes,<sup>3</sup> Salvatore Savasta,<sup>2,1</sup> and Franco Nori<sup>1,2,5</sup>

<sup>1</sup>Dipartimento di Scienze Matematiche e Informatiche, Scienze Fisiche e Scienze della Terra, Università di Messina, I-98166 Messina, Italy

<sup>2</sup>Theoretical Quantum Physics Laboratory, RIKEN, Wako-shi, Saitama 351-0198, Japan

<sup>3</sup>Department of Physics, Engineering Physics and Astronomy, Queen's University, Kingston, Ontario, Canada K7L 3N6

<sup>4</sup>Department of Applied Physics, Stanford University, Stanford, California 94305, USA

<sup>5</sup>Physics Department, The University of Michigan, Ann Arbor, Michigan 48109-1040, USA



(Received 20 December 2021; accepted 23 March 2022; published 20 April 2022)

The prototypical system constituted by a two-level atom interacting with a quantized single-mode electromagnetic field is described by the quantum Rabi model (QRM). The QRM is potentially valid at any light-matter interaction regime, ranging from the weak (where the decay rates exceeds the coupling rate) to the deep strong coupling (where the interaction rate exceeds the bare transition frequencies of the subsystems). However, when reaching the ultrastrong coupling regime, several theoretical issues may prevent the correct description of the observable dynamics of such a system: (i) the standard quantum optics master equation fails to correctly describe the interaction of this system with the reservoirs; (ii) the correct output photon rate is no longer proportional to the intracavity photon number; and (iii) they appear to violate gauge invariance. Here, we study the photon flux emission rate of this system under the incoherent excitation of the two-level atom for any light-matter interaction strength and consider different effective temperatures. The dependence of the emission spectra on the coupling strength is the result of the interplay between energy levels, matrix elements of the observables, and the density of states of the reservoirs. Within this approach, we also study the occurrence of light-matter decoupling in the deep strong-coupling regime and show how all of the obtained results are gauge invariant.

DOI: 10.1103/PhysRevResearch.4.023048

### I. INTRODUCTION

The quantum Rabi model (QRM) provides the simplest full quantum description of light-matter interaction. It is also one of the most well studied models in quantum optics, and a cornerstone of cavity quantum electrodynamics (cavity QED). The quantum Rabi Hamiltonian describes the dipolar interaction of a two-level system (TLS) or qubit with a single quantized mode of an electromagnetic resonator. It was first introduced by Jaynes and Cummings [1] in order to compare the semiclassical model, previously introduced by Rabi [2], with a full quantum model. To solve the model, the rotating wave approximation (RWA) is commonly introduced. In this approximation, known as the Jaynes-Cummings model (JCM), the counter-rotating terms are neglected. This is a valid approximation for the near-resonance case and when the light-matter coupling rate is much smaller than the resonance frequency of the TLS or, equivalently, of the quantized cavity mode. These conditions are fulfilled in several experimental

settings [3,4]. The RWA may also fail for describing the optical pumping, when the excitation field is sufficiently strong or for a nonlinear short pulse excitations with several carrier cycles [5].

Despite its simplicity, the QRM is able to describe a wide variety of light-matter quantum systems and gives rise to a great diversity of behaviors and effects, depending on the relative magnitude of the light-matter coupling strength. However, the description and the analysis of experiments on systems which can be potentially modeled by the quantum Rabi Hamiltonian require additional theoretical tools. For example, it is necessary to take into account the interaction of both the TLS and cavity photons with the external environment (thermal reservoirs) [6]. Of course, in the absence of such interactions, basic features such as the excitation of the system components, dissipation and decoherence effects, and the detection of photons outside the cavity cannot be described properly. Even the definition of the different light-matter interaction regimes requires one to include the interaction of the system components with their reservoirs.

In weak-coupling regime of cavity QED, dissipation is stronger than the intrinsic coherent coupling between matter and the light. Such a regime has led to various applications, e.g., exploiting the well-known Purcell effect [7] has allowed for breakthroughs in quantum technologies such as low-threshold solid-state lasers [8] and single-photon emitters [9,10]. These effects allow for the engineering of the spontaneous emission rate of an emitter, by tailoring its photonic environment. Indeed, resonant electromagnetic

\*These authors contributed equally to this work.

†alberto.mercurio@unime.it

‡vincenzo.macri@riken.jp

resonators with a narrow density of states can greatly enhance the efficiency of photonic devices. Going beyond weak coupling, the strong-coupling regime is characterized by lower losses in the system, allowing for the observation of effects such as vacuum Rabi oscillations [11], manifested by the coherent oscillatory exchange of energy between light and matter. Such effects are already being exploited in second-generation quantum technologies [12,13]. In this strong-coupling regime, however, the light-matter coupling rate, remains much lower than the bare resonance frequencies, so that both the weak and the strong-coupling regime can be adequately described by the JCM.

If the quantum light–matter interaction strength reaches a non-negligible fraction of the transition frequency of the components, the system enters the so-called ultrastrong coupling (USC) regime. In this regime, the interaction can significantly change the system properties. For example, the ground state of the system contains non-negligible virtual photons and virtual matter excitations. In the past decade, USC effects between light and matter has transitioned from a theoretical idea to an experimental reality. Nowadays, this regime has been achieved in a great variety of systems and settings [3,4]. The experimental progress in USC physics has motivated many theoretical studies showing interesting new effects enabled or boosted by this regime [14–42]. Several studies explore higher-order processes in the USC regime, where the number of excitations is not conserved [43–48], such as multiphoton Rabi oscillations [49] and a single photon exciting multiple atoms [50,51].

When the light-matter interaction strength increases even further, a regime where the coupling strength exceeds the resonant frequencies of the material and/or of the quantized light modes can be achieved [30]—the deep strong-coupling (DSC) regime. One of the most interesting effects predicted in this regime is the effective decoupling between light and matter [52,53]. A striking consequence of such a counterintuitive phenomenon is that the Purcell effect is reversed and the spontaneous emission rate, usually thought to increase with the light-matter coupling strength, tends to vanish for sufficiently large couplings. Such a result has been predicted considering bosonic matter excitations interacting with a multimode optical resonator (generalized Hopfield model), and using the Coulomb gauge. Recently, the decoupling effect has been predicted for any light-matter system obtained with the minimal-coupling replacement of the electronic momentum [53]. Adopting the so-called asymptotic decoupling frame, the authors showed that the electronic system tends to localize when the coupling increases, since the effective mass tends to increase. A first confirmation of this prediction has been obtained using three-dimensional crystals of plasmonic nanoparticles [54].

In subsequent work [55], this effect has also been studied considering a single superconducting qubit interacting with a multimode electromagnetic resonator. In circuit QED, for a qubit interacting with a superconducting waveguide, a microscopic treatment of the light-matter coupling gives rise to a diamagnetic term, analogous to the  $A^2$  term of the minimal-coupling Hamiltonian. Using this spin-boson Hamiltonian, it has been shown that the spontaneous emission rate of the two-level system decreases with the intensity of the  $A^2$  term,

without the need to be in the DSC regimes. The results in Refs. [52,55] suggest that the diamagnetic term plays a key role in determining the light-matter decoupling effect. However, some questions remains open. Indeed, the presence of the diamagnetic term is gauge relative (e.g., it disappears in the dipole gauge); moreover, the validity of the Coulomb gauge when describing truncated atomic systems has been questioned [56–58].

Recently, some gauge issues have been solved. In particular, it has been shown how to obtain the correct quantum Rabi and Dicke Hamiltonians in the Coulomb gauge [59–62]. It has also been shown how to derive a gauge-invariant master equation and obtain gauge-invariant emission spectra [63]. Throughout this article, we will use these recent developments. Specifically, we provide a unified picture of light emission under incoherent pumping of the QRM, from the weak to the deep strong light-matter interaction. When the light-matter coupling strength spans from the very weak to the deep strong-coupling regimes, the spectrum of the QRM, while initially quasiharmonic, becomes strongly anharmonic at higher couplings. Then, after reaching the deep strong limit, its behavior tends back towards harmonicity.

While in the weak-coupling regime, neglecting the counter-rotating terms and using the standard quantum optics master equation typically provides accurate results, in the USC regime this master equation fails to describe correctly the emission spectra. This problem can be partly solved by introducing the master equation in the dressed basis [64], an approach which includes the interaction between the system components in the derivation of the dissipators. However, this powerful approach can also fail in describing the emission of the QRM in both the weak and deep strong-coupling regimes. To solve these problems, we study the incoherent emission of the system at any coupling strength, using a dressed-state generalized master equation (GME) working for systems displaying both harmonic, quasiharmonic, and anharmonic spectra [65]. Moreover, we take particular care to derive a gauge-invariant GME, to ensure the gauge invariance of the obtained emission rates and spectra [63].

In Sec. II, we first provide a description of the QRM in both the Coulomb and multipolar gauges, and then present the GME approach which we will use for all the calculations. A detailed description of the derivation is provided in the Appendixes (see also Ref. [63]). The numerical calculations and their analysis are presented in Sec. III. There, we show numerically calculated cavity and qubit photon flux emission rates and spectra as a function of the normalized light-matter coupling strength, obtained for different effective temperatures and considering also the cavity-qubit detuning. Finally, in Sec. IV, we give our conclusions.

In addition, the main theoretical framework used to develop all the results is fully explained in the Appendixes. In Appendix A we model the cavity- and qubit-bath interaction by using the gauge principle, while in Appendix B we provide a demonstration of the gauge invariance of the GME. The positive cavity-qubit detuning case can be found in Appendix C, while, in order to highlight the differences between our results based on a gauge-consistent GME, and some other standard methods, in Appendix D, we present (i) results obtained using the JC model and the standard

quantum optics master equation, and (ii) results obtained using a dressed master equation with the post-trace rotating-wave approximation [64].

## II. DISSIPATIVE QUANTUM RABI MODEL

In this section, we describe the open QRM, thus including the interaction of the light and matter components with their respective reservoirs. We consider models in both the Coulomb and the multipolar gauge (within the dipole approximation), to show equivalence and verify gauge-invariant observables.

### A. Quantum Rabi model in the Coulomb gauge

The quantum Rabi Hamiltonian in the Coulomb gauge can be written as ( $\hbar = 1$ ) [59]

$$\hat{\mathcal{H}}_R = \omega_c \hat{a}^\dagger \hat{a} + \frac{\omega_q}{2} \{ \hat{\sigma}_z \cos[2\eta(\hat{a} + \hat{a}^\dagger)] \\ + \hat{\sigma}_y \sin[2\eta(\hat{a} + \hat{a}^\dagger)] \}, \quad (1)$$

where  $\hat{a}$  ( $\hat{a}^\dagger$ ) is the photon annihilation (creation) operator and  $\hat{\sigma}_{x,y,z}$  are Pauli matrices. The parameters  $\omega_c$  and  $\omega_q$  represent the cavity and the qubit resonance frequencies, respectively, while  $\eta = g/\omega_c$  is the normalized light-matter coupling strength.

The Hamiltonian  $\hat{\mathcal{H}}_R$  can be obtained starting from the light-matter Hamiltonian in the absence of interaction  $\hat{\mathcal{H}}_0 = \hat{\mathcal{H}}_q + \hat{\mathcal{H}}_{ph}$ , where  $\hat{\mathcal{H}}_q = \omega_q \hat{\sigma}_z / 2$  and  $\hat{\mathcal{H}}_{ph} = \omega_c \hat{a}^\dagger \hat{a}$ , by applying a suitable unitary transformation (generalized minimal-coupling transformation) to  $\hat{\mathcal{H}}_q$  only [59,61]. Specifically,

$$\hat{\mathcal{H}}_R = \hat{U} \hat{\mathcal{H}}_q \hat{U}^\dagger + \hat{\mathcal{H}}_{ph}, \quad (2)$$

where

$$\hat{U} = \exp[i\eta(\hat{a} + \hat{a}^\dagger)\hat{\sigma}_x]. \quad (3)$$

We observe that, in the Coulomb gauge, the canonical field momentum is not modified by the interaction with the matter component, i.e.,  $\Pi = -\epsilon_0 \hat{E}$  ( $\epsilon_0$  is the vacuum permittivity), such that, in this framework, the electric-field operator can be written as

$$\hat{E} = i\omega_c A_0 (\hat{a} - \hat{a}^\dagger), \quad (4)$$

where  $A_0$  is the zero-point-fluctuation amplitude of the field coordinate. For simplicity we assume a simple one-dimensional model, but the formalism can be easily generalized to three dimensions.

Regardless of the chosen gauge, when the normalized coupling strength becomes significantly large, all the eigenstates become *dressed* by virtual excitations (owing to the presence of the counter-rotating terms) [66], and complications arise in the theoretical description [3]. Consequently, dissipation effects, input-output relationships, and photodetection rates [67,68] cannot be introduced adequately by using the standard tools of quantum optics in the usual fashion. For example, considering a given quantum state of the system  $\hat{\rho}(t)$  (i.e., the density operator of the light-matter system at time  $t$ ), the photon rate measured by a broadband point-like detector in the resonator is different from  $\langle \hat{a}^\dagger \hat{a} \rangle_t \equiv \text{Tr}[\hat{a}^\dagger \hat{a} \hat{\rho}(t)]$ . Instead,

it is proportional to the expectation value  $W_c(t) = \langle \hat{\mathcal{E}}^- \hat{\mathcal{E}}^+ \rangle_t \equiv \text{Tr}[\hat{\mathcal{E}}^- \hat{\mathcal{E}}^+ \hat{\rho}(t)]$ . Here,  $\hat{\mathcal{E}}^+$  [ $\hat{\mathcal{E}}^- = (\hat{\mathcal{E}}^+)^\dagger$ ] is proportional to the positive-frequency (negative-frequency) electric-field operator, and the expectation value is taken considering quantum states calculated in the Coulomb gauge (dressed-state representation).

Specifically, the positive-frequency electric-field operator is obtained from

$$\hat{\mathcal{E}}^+ = i \sum_{k>j} \langle j | (\hat{a} - \hat{a}^\dagger) | k \rangle | j \rangle \langle k |, \quad (5)$$

where  $|j\rangle$  are the energy eigenstates of the Hamiltonian in Eq. (1) with eigenvalues  $\omega_j$  ordered so that  $k > j$  for  $\omega_k > \omega_j$ . Using the relationship [69]

$$\omega_c \langle j | (\hat{a} - \hat{a}^\dagger) | k \rangle = \omega_{kj} \langle j | (\hat{a} + \hat{a}^\dagger) | k \rangle, \quad (6)$$

where  $\omega_{kj} = \omega_k - \omega_j$ , it is also possible to rewrite Eq. (5) as

$$\hat{\mathcal{E}}^+ = i \sum_{k>j} \frac{\omega_{kj}}{\omega_c} \langle j | (\hat{a} + \hat{a}^\dagger) | k \rangle | j \rangle \langle k |. \quad (7)$$

Note that Eq. (6) remains valid even in the presence of very strong light-matter interactions and/or optical nonlinearities.

By using the simple input-output theory [70], results analogous to  $W_c(t)$  can be obtained for the rate  $\dot{W}_c^{\text{out}}(t)$  of emitted photons detected by a detector placed outside the cavity [71,72]. However, the output field operators can display a different dependence on  $\omega_{kj}$ , arising from the density of states of the output modes and from the frequency dependence of the coupling coefficient, which (for example) depends on the mirror reflectivity in a standard microcavity. More generally, the output field operator, in the Coulomb gauge, can be written as

$$\hat{\mathcal{E}}_{\text{out}}^+ = i \sum_{k>j} \alpha(\omega_{kj}) \langle j | (\hat{a} + \hat{a}^\dagger) | k \rangle | j \rangle \langle k |, \quad (8)$$

where the function  $\alpha(\omega)$  encodes the specific, model-dependent dependence on the frequency. A more rigorous input-output theory can be formulated in terms of quantized quasinormal modes [73–75].

Analogously, it is possible to define the field operators describing the qubit emission  $W_q(t) = \langle \hat{\mathcal{S}}^- \hat{\mathcal{S}}^+ \rangle_t$ , where

$$\hat{\mathcal{S}}^+ = i \sum_{k>j} \alpha_q(\omega_{kj}) \langle j | \sigma_x | k \rangle | j \rangle \langle k |. \quad (9)$$

Considering a standard cavity QED system, for example, the cavity emission rate corresponds to the photon flux escaping one of the mirrors, while the qubit emission rate corresponds to the spontaneous emission directly from the qubit, which can be collected by a detector placed orthogonally to the axis connecting the two mirrors [76,77].

In the following, we assume both  $\alpha_c(\omega_{kj}) = \omega_{kj}/\omega_c$  (corresponding to  $\hat{\mathcal{E}}_{\text{out}}^+ = \hat{\mathcal{E}}^+$ ) and  $\alpha_q(\omega_{kj}) = \omega_{kj}/\omega_q$  to be linearly dependent on the transition frequencies. A different choice will give rise to similar spectra with different relative heights of the spectral lines. Notice that photodetection is an energy absorption process, thus it is reasonable to assume photon detection rates which tend to zero with frequencies  $\omega \rightarrow 0$ . Naturally, any realistic analysis covering a very large frequency range should also include dispersion in the material

model. Including the latter, however, would make the study system dependent going beyond the aim of the present general framework.

### B. Quantum Rabi model in the dipole gauge

The quantum Rabi Hamiltonian can also be expressed in the dipole gauge, which yields the form

$$\hat{\mathcal{H}}'_R = \omega_c \hat{a}^\dagger \hat{a} + \frac{\omega_q}{2} \hat{\sigma}_z - i\eta\omega_c (\hat{a} - \hat{a}^\dagger) \hat{\sigma}_x + \omega_c \eta^2 \hat{\sigma}_x^2, \quad (10)$$

where  $\hat{\sigma}_x^2 = \hat{I}$  gives the identity operator. Hence, the last term induces only a rigid shift of all the energy levels. To be clear, by dipole gauge, we mean the multipolar gauge after the dipole approximation [78,79]. Light-matter Hamiltonians in the multipolar or dipole gauge can be obtained from the Coulomb gauge (minimal-coupling replacement), after a unitary Power-Zienau-Woolley (PZW) transformation [80].

The last term in Eq. (10) is often disregarded, since it has no dynamical consequences. In the following, when needed, as for the Hamiltonian in the dipole gauge  $\hat{\mathcal{H}}'_R$ , we will use primed symbols to indicate gauge-relative quantities in the dipole gauge. By considering a fixed polarization in the single-mode approximation, the field coordinate corresponding to the vector potential can be expressed as  $\hat{A} = A_0(\hat{a} + \hat{a}^\dagger)$ . In the dipole gauge, the field conjugate momentum is modified by the interaction with the matter system, and it is proportional to the electric displacement (induction) field,

$$\hat{\Pi}' = -\hat{D} = -i\varepsilon_0\omega_c A_0(\hat{a} - \hat{a}^\dagger). \quad (11)$$

Thus, the electric-field operator cannot be expanded in terms of photon operators only. Indeed, due to the fact that  $\hat{D} = \varepsilon_0 \hat{E}' + \hat{P}$  (for a dipole in free space), where  $\hat{P}$  is the electric polarization, the electric-field operator in the dipole gauge has to be expanded as

$$\hat{E}' = i\omega_c A_0(\hat{a}' - \hat{a}'^\dagger), \quad (12)$$

where (see Ref. [62])

$$\hat{a}' = \hat{R}\hat{a}\hat{R}^\dagger = \hat{a} + i\eta\hat{\sigma}_x, \quad (13)$$

and

$$\hat{R} = \hat{U}^\dagger = \exp[-i\eta(\hat{a} + \hat{a}^\dagger)\hat{\sigma}_x]. \quad (14)$$

This unitary operator essentially implements the PZW transformation for a truncated TLS model and in the dipole approximation [61]. Of course, the different representations provide the same energy levels for the light-matter system. They also provide identical expectation values if operators and quantum states are both properly transformed [62]. We observe that the operators  $\hat{a}'$  and  $\hat{a}'^\dagger$  satisfy the same commutation relations of the bosonic operators  $\hat{a}$  and  $\hat{a}^\dagger$ . Moreover, since  $\hat{a}' + \hat{a}'^\dagger = \hat{a} + \hat{a}^\dagger$ , the vector potential can also be expressed as  $\hat{A} = A_0(\hat{a}' + \hat{a}'^\dagger)$ . We observe that, in the dipole gauge,  $\hat{a}'$  and  $\hat{a}'^\dagger$  (instead of  $\hat{a}$  and  $\hat{a}^\dagger$ ) describe the creation and annihilation of the field quanta, as is clear from Eq. (12).

The quantum Rabi Hamiltonians in Eqs. (1) and (10) are related by a gauge transformation, implemented by the unitary operator in Eq. (14):

$$\hat{\mathcal{H}}'_R = \hat{R}\hat{\mathcal{H}}_R\hat{R}^\dagger. \quad (15)$$

The photon rate measured by a broadband point-like detector in the resonator can be expressed also in the dipole gauge as  $W'_c(t) = \langle \hat{\mathcal{E}}'^- \hat{\mathcal{E}}'^+ \rangle_t'$ , where the expectation values are calculated using the eigenstates  $|j'\rangle$  of Eq. (10). Therefore,  $\hat{\mathcal{E}}'^+$  is now proportional to the positive-frequency electric-field operator in the dipole gauge,

$$\hat{\mathcal{E}}'^+ = i \sum_{k>j} \langle j' | (\hat{a}' - \hat{a}'^\dagger) | k' \rangle | j' \rangle \langle k' |. \quad (16)$$

From Eq. (13), clearly we see that the photon operators are not gauge invariant. Thus, in order to obtain correct results in the dipole gauge [62], it is essential to properly take into account how these operators change under the  $\hat{U}$  transformation [see Eq. (13)].

Choosing the dipole gauge, without transforming the photonic operators accordingly, can lead to an erroneous evaluation of the emitted photon rate, as shown in Sec. III. Specifically, an incorrect photon rate is obtained by using  $\hat{a}$  ( $\hat{a}^\dagger$ ) instead of  $\hat{a}'$  ( $\hat{a}'^\dagger$ ) in the dipole gauge. In this case, the photon rate becomes

$$\tilde{W}'_c = \langle \hat{\mathcal{E}}'_w^- \hat{\mathcal{E}}'_w^+ \rangle', \quad (17)$$

where

$$\hat{\mathcal{E}}'_w^+ = i \sum_{k>j} \langle j' | (\hat{a} - \hat{a}^\dagger) | k' \rangle | j' \rangle \langle k' |. \quad (18)$$

Also note,  $\tilde{W}'_c \neq W'_c = W_c$  (see Sec. III).

The useful relationship shown by Eq. (6) can be appropriately transformed in the dipole gauge as

$$\omega_c \langle j' | (\hat{a}' - \hat{a}'^\dagger) | k' \rangle = \omega_{kj} \langle j' | (\hat{a}' + \hat{a}'^\dagger) | k' \rangle, \quad (19)$$

such that

$$\hat{\mathcal{E}}'^+ = i \sum_{k>j} \frac{\omega_{kj}}{\omega_c} \langle j' | (\hat{a}' + \hat{a}'^\dagger) | k' \rangle | j' \rangle \langle k' |, \quad (20)$$

and we also have

$$\langle j' | (\hat{a}' + \hat{a}'^\dagger) | k' \rangle = \langle j | (\hat{a} + \hat{a}^\dagger) | k \rangle. \quad (21)$$

### C. Theoretical description of losses and quantum noise

To calculate emission rates and emission spectra of the QRM, from the weak to the DSC regime, we describe the dissipative system dynamics considering a GME in the dressed basis [65],

$$\dot{\hat{\rho}} = -i[\hat{\mathcal{H}}_R, \hat{\rho}] + \mathcal{L}_g \hat{\rho}, \quad (22)$$

where the dissipator  $\mathcal{L}_g$  contains two contributions  $\mathcal{L}_g = \mathcal{L}_g^c + \mathcal{L}_g^q$ , arising from the cavity-bath (c) and the qubit-bath (q) interaction [see Appendix B and in particular Eq. (B2)]. It remains valid at any light-matter coupling strength. By using this approach, we also include the interaction of the matter and light components of the system with individual reservoirs that can be at different temperatures [see Eq. (B3)].

Starting from a gauge-invariant approach (see Appendix B), the obtained photonic and atomic decay rates associated with given system transitions can be written

as

$$\Gamma_{kj}^c = \kappa \frac{\omega_{kj}}{\omega_c} |\langle j | \hat{a} + \hat{a}^\dagger | k \rangle|^2, \quad \Gamma_{kj}^q = \gamma \frac{\omega_{kj}}{\omega_q} |\langle j | \hat{\sigma}_x | k \rangle|^2, \quad (23)$$

where  $\kappa$  and  $\gamma$  are the bare (in the absence of cavity-atom coupling) loss rates for the photon and the atom, and Ohmic reservoirs have been considered (i.e., the rates scale linearly with frequency). Since the matrix elements in Eq. (23) are gauge invariant, then  $\Gamma_{kj}^{c(q)} = \Gamma_{k'j'}^{c(q)}$ . As done before, we label the quantum states and operators in the dipole gauge with the prime superscript.

These *gauge-invariant* decay rates have been derived starting from cavity and qubit reservoir interactions obtained by invoking the gauge principle (see Appendix A). This also gives rise to a gauge-invariant GME (see Appendix B), which, in turns, provides gauge-invariant emission rates and spectra (see Sec. II D).

#### D. Formulas for cavity and qubit emission spectra

In addition to cavity and qubit emission rates, we also present emission spectra, which allows one to obtain information on the frequency of the emitted photons and, indirectly, on the system dynamics under incoherent excitation (for example). The steady-state cavity and qubit emission spectra (obtained from the steady-state density operator  $\hat{\rho}_{ss}$  by applying the quantum regression theorem [70,76,81]) can be defined as

$$\begin{aligned} \tilde{S}_c(\omega) &= \text{Re} \int_0^\infty d\tau e^{-i\omega\tau} \langle \hat{\mathcal{E}}^-(t+\tau) \hat{\mathcal{E}}^+(t) \rangle_{ss}, \\ \tilde{S}_q(\omega) &= \text{Re} \int_0^\infty d\tau e^{-i\omega\tau} \langle \hat{\mathcal{S}}^-(t+\tau) \hat{\mathcal{S}}^+(t) \rangle_{ss}. \end{aligned} \quad (24)$$

Note that the above definition is valid only when considering steady state (ss). In the USC regime, true steady state is achieved only under incoherent pumping. Under coherent drive, the counter-rotating terms often determine the presence of oscillations in the signals, even for times much longer than coherence times. In this case the spectra have to be defined introducing an additional time integration [63].

Instead of Eq. (24), we adopt slightly different formulas for the spectra. Actually, the frequency of photons detected after a spectrum analyzer tuned at a frequency  $\omega$  is just  $\omega$  and not  $\omega_{kj}$ , even if they originate from a specific downward transition  $|k\rangle \rightarrow |j\rangle$  (which, however, is broadened by the interaction of the system with the reservoirs). Hence, it is somewhat more accurate to replace  $\omega_{kj}$  with  $\omega$  in the emission spectra formulas. In this way, in the low-frequency limit, the spectra goes to zero as expected. However, this replacement can affect the high-frequency behavior of the spectra, especially when some cutoff mechanism is not introduced.

By making use of Eqs. (6) and (19), and by applying the replacement  $\omega_{kj} \rightarrow \omega$ , we obtain

$$\begin{aligned} S_c(\omega) &= \frac{\omega^2}{\omega_c^2} \text{Re} \int_0^\infty d\tau e^{-i\omega\tau} \langle \underline{\hat{\mathcal{E}}}^-(t+\tau) \underline{\hat{\mathcal{E}}}^+(t) \rangle_{ss}, \\ S_q(\omega) &= \frac{\omega^2}{\omega_q^2} \text{Re} \int_0^\infty d\tau e^{-i\omega\tau} \langle \underline{\hat{\mathcal{S}}}^-(t+\tau) \underline{\hat{\mathcal{S}}}^+(t) \rangle_{ss}, \end{aligned} \quad (25)$$

where

$$\begin{aligned} \underline{\hat{\mathcal{E}}}^- &= -i \sum_{k>j} \langle k | (\hat{a}^\dagger + \hat{a}) | j \rangle | k \rangle \langle j |, \\ \underline{\hat{\mathcal{S}}}^- &= -i \sum_{k>j} \langle k | \hat{\sigma}_x | j \rangle | k \rangle \langle j |. \end{aligned} \quad (26)$$

The results obtained using Eqs. (24) and (25) are very similar, and small differences can emerge only on a logarithmic scale.

### III. NUMERICAL RESULTS

In this section, we present numerical calculations for the photon emission rates and spectra for both the cavity and the qubit, under qubit incoherent pumping, as a function of the normalized coupling strength  $\eta$ . A similar analysis has been carried out in the strong-coupling regime using the JC model and the standard quantum optics master equation, which are appropriate in this regime [77].

The incoherent excitation of the qubit is described by coupling it with a thermal reservoir at a given effective temperature  $T_q \equiv K_B T / \omega_q \neq 0$  (here  $K_B$  is the Boltzmann constant). All the results have been obtained assuming a zero-temperature ( $T_c = 0$ ) cavity reservoir, so that the cavity emission originates from the interaction with the qubit.

The eigenstates of the quantum Rabi Hamiltonian are obtained by standard numerical diagonalization in a truncated, but sufficiently large, finite-dimensional, Hilbert space. Specifically, we consider the Hilbert space resulting from the tensor product of the qubit basis  $\{|g\rangle, |e\rangle\}$ , and the basis constituted by the  $N+1$  photonic Fock states up to the  $N$ -photon state  $|N\rangle$ . The truncation number  $N$  is chosen in order to ensure that the lowest  $M$  energy eigenvalues and corresponding eigenvectors of interest are not appreciably modified when increasing  $N$ . All the results are obtained solving the GME in Eq. (22), for the density matrix of the cavity-qubit in the dressed basis, including the lowest  $M$  energy levels. The truncation number  $M$  is chosen to reach convergence. Specifically, we check that the results (emission rates and spectra) do not notably change when increasing  $M$ .

In the following, where more convenient, we use a different notation for the eigenstates of the QRM, in analogy with the notation used to label the eigenstates of the JCM. At zero detuning [ $\Delta \equiv (\omega_c - \omega_q)/\omega_q = 0$ ], the excited eigenstates of the JC Hamiltonian can be written as  $|n_\pm\rangle = (|n, g\rangle \pm |n-1, e\rangle)/\sqrt{2}$ . The eigenstates of the QRM, beyond the strong-coupling regime do not display the same simple structure. Here, when useful, we indicate them by generalizing the above JC notation by introducing a tilde. With this notation, the state  $|\tilde{0}\rangle$  denotes the ground state, and  $|\tilde{n}_\pm\rangle$  describes an eigenstate of the quantum Rabi Hamiltonian. Note that  $|\tilde{n}_\pm\rangle$  tends to the corresponding JC state  $|n_\pm\rangle$  for  $\eta \ll 1$ . With this notation, the energy eigenstates maintain their parity (corresponding to the parity of the integer number  $\tilde{n}$ ) independently of the value of  $\eta$ .

All the numerical calculations involving the master equation have been obtained using  $\gamma/\omega_q = 10^{-4}$  and  $\kappa/\omega_q = 10^{-3}$  and using QUTIP under Python [82,83].

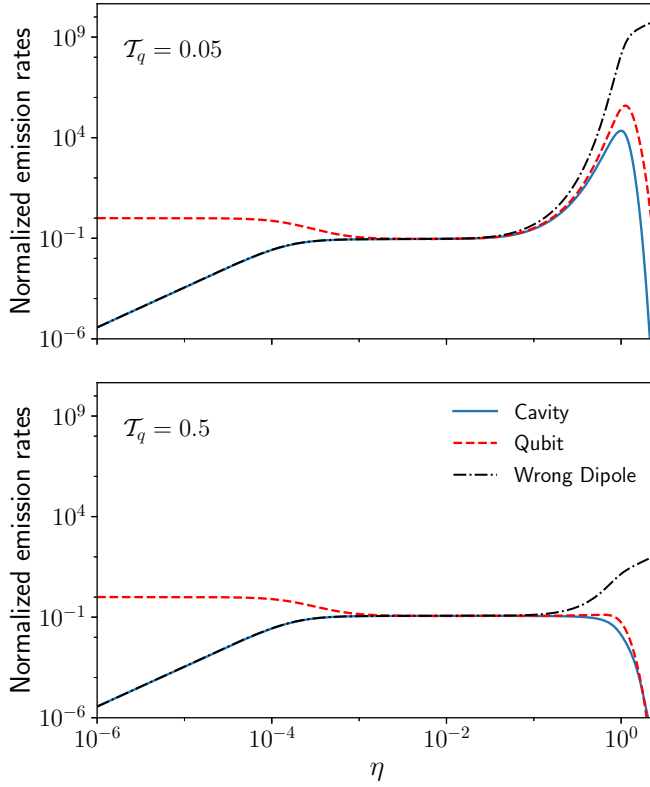


FIG. 1. Numerically calculated cavity and qubit steady-state photon emission flux rates (normalized with respect to the qubit emission rate  $W_q^0$  calculated for  $\eta = 0$ )  $\mathcal{W}_c = W_c/W_q^0$  (blue continuous curves), and  $\mathcal{W}_q = W_q/W_q^0$  (red dashed) versus the light-matter normalized coupling strength  $\eta$ . We used  $\Delta = 0$  (zero cavity-qubit detuning). Black-point-dashed curves indicate the cavity emission rates  $\tilde{\mathcal{W}}_c = \tilde{W}_c/W_q^0$  calculated in the dipole gauge, using the *wrong* positive-frequency electric-field operator in Eq. (18). The upper panel (a) has been obtained for  $T_q = 5 \times 10^{-2}$ , the lower one (b) for  $T_q = 5 \times 10^{-1}$ .

### A. Zero cavity-qubit detuning

Here, we present the results obtained analyzing emission rates and spectra at zero cavity-qubit detuning  $\Delta \equiv (\omega_c - \omega_q)/\omega_q = 0$ .

#### 1. Cavity and qubit emission rates

Figure 1 shows the numerically calculated cavity and qubit steady-state photon emission flux rates (normalized with respect to the qubit emission rate  $W_q^0$  for  $\eta = 0$ )  $\mathcal{W}_c = W_c/W_q^0$  (blue continuous curve), and  $\mathcal{W}_q = W_q/W_q^0$  (red dashed curve) versus the light-matter normalized coupling strength  $\eta$ , calculated at two different effective temperatures of the qubit reservoir. The black-point-dashed curve indicates the cavity emission rates  $\tilde{\mathcal{W}}_c = \tilde{W}_c/W_q^0$  calculated in the dipole gauge, using the *wrong* positive-frequency electric-field operator in Eq. (18). We first observe that, the methods discussed in Sec. II allow us to calculate emission rates for very different values of  $\eta$ , within a unified theoretical framework from the weak to the DSC regimes.

Figure 1 clearly shows that, at low coupling strengths (i.e., weak-coupling regime), a continuous increase of the

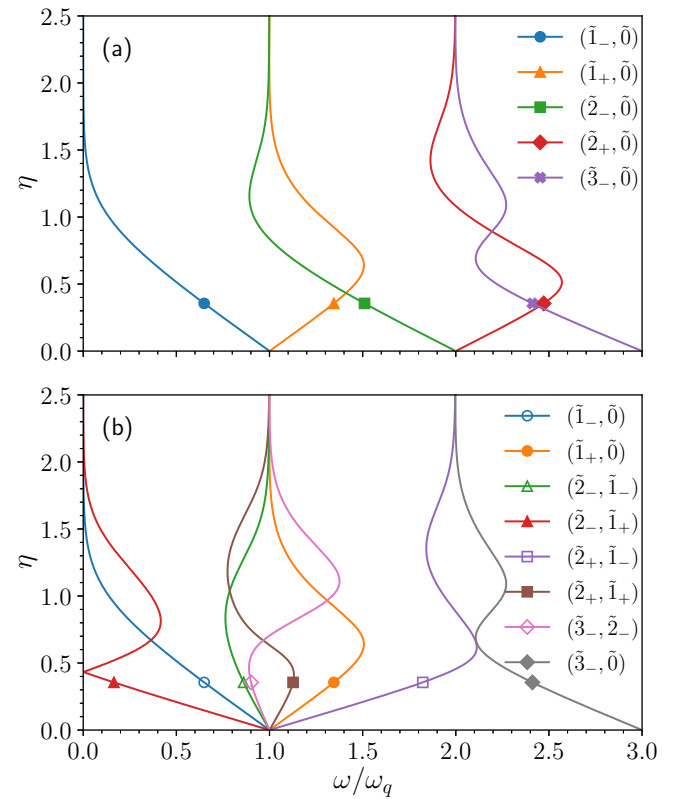


FIG. 2. Normalized energy levels and transition energies versus  $\eta$ , for  $\Delta = 0$ . (a) Lowest normalized energy levels (with the ground-state energy as reference)  $|\omega_{j\pm} - \omega_0|/\omega_q$  of the QRM. (b) Normalized parity-allowed transition energies  $|\omega_k - \omega_j|/\omega_q$  for the lowest eigenstates of the QRM.

cavity-emission rate with increasing  $\eta$  occurs for both, very low and higher effective temperatures (Purcell effect). When the system approaches the SC regime [ $\omega_q\eta \simeq (\kappa + \gamma)/4$ ] a plateau is reached, in which the emission rate is equally shared between the atom and the cavity. By increasing further the coupling beyond the onset of USC ( $\eta > 0.1$ ), a strong enhancement of both the cavity and qubit emission can be observed at low temperature  $T_q = 5 \times 10^{-2}$  [Fig. 1(a)]. It originates from the decrease of the transition frequency  $\omega_{1\perp,0}$  between the lowest excited state and the ground state for increasing values of  $\eta$  [see Fig. 2(b)]. The strong decrease of  $\omega_{1\perp,0}$  enables the increase of the occupancy of the state  $|1\perp\rangle$  at very low effective temperatures. Such a population growth determines an increase in the emission rate (of photons at frequency  $\omega_{1\perp,0}$ ), which can be observed in Fig. 1(a). The same behavior is not observed at a significantly higher temperature [Fig. 1(b)]. In this case, the state  $|1\perp\rangle$  can already be populated at small values of  $\eta$ .

When increasing  $\eta$  to values beyond the DSC regime ( $\eta > 1$ ), then both  $\mathcal{W}_c$  and  $\mathcal{W}_q$  decrease rapidly. This behavior can be understood by looking at the energy eigenvalues in Fig. 2(a) in the large- $\eta$  limit. Indeed, in this regime, all the transition frequencies tend to become flat, equally spaced, and two-by-two quasidegenerate. Theoretical analysis [62] shows that, beyond the DSC regime, the quasidegenerate light-matter eigenstates tend to factorize as  $|n, g\rangle$  and  $|n, e\rangle$ , so that the

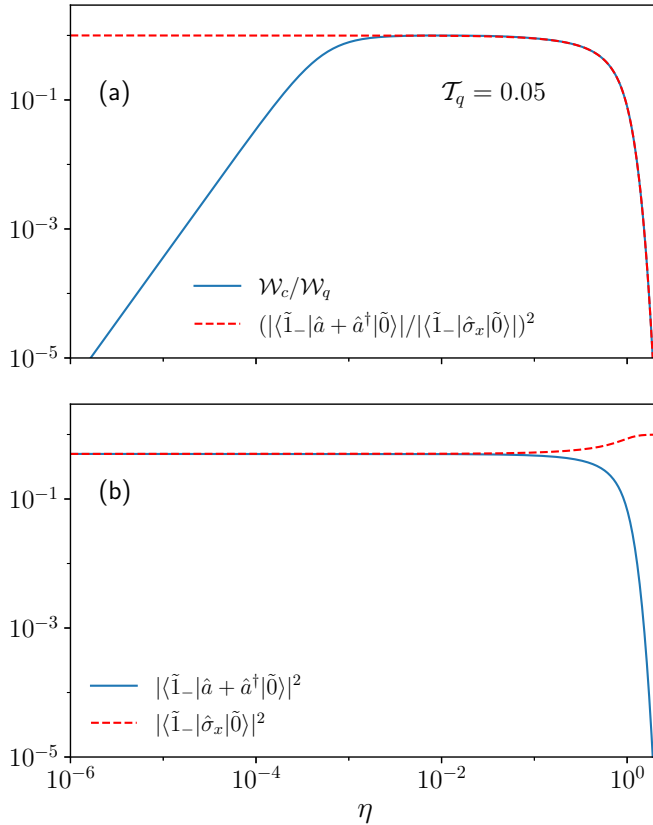


FIG. 3. (a) Ratio of the cavity to the qubit emission rates  $\mathcal{W}_c/\mathcal{W}_q$ , for detuning  $\Delta = 0$ ,  $T_q = 5 \times 10^{-2}$ , as a function of the normalized coupling strength  $\eta$ . The blue continuous curve describes the numerically calculated ratio, while the red-dashed one is the corresponding analytical approximated result  $\mathcal{W}_c/\mathcal{W}_q \simeq |\langle \tilde{1}_- | (\hat{a} + \hat{a}^\dagger) | \tilde{0} \rangle|^2 / |\langle \tilde{1}_- | \hat{\sigma}_x | \tilde{0} \rangle|^2$  [see Eq. (27)]. The two curves tend to coincide for  $\eta > 10^{-3}$ . In panel (b), the square modules of the matrix elements that determine the approximate ratio in panel (a) are shown.

system tends to decouple from the qubit reservoir ( $\Gamma_{kj}^q \rightarrow 0$ ) and cannot be significantly excited. Specifically, the matrix elements  $\langle j | \hat{\sigma}_x | k \rangle$  are different from zero only for states such that  $\omega_{kj} \rightarrow 0$ . As a consequence,  $\Gamma_{kj}^q \rightarrow 0$ .

We also notice that, in the large- $\eta$  limit, especially at low temperatures [see Fig. 1(a)], the cavity emission rate  $\mathcal{W}_c$  goes to zero more rapidly than  $\mathcal{W}_q$ . This feature is shown more clearly in Fig. 3(a), where the ratio  $\mathcal{W}_c/\mathcal{W}_q$  is displayed (blue continuous curve). The figure shows the standard Purcell-like dependence in the weak-coupling regime, while  $\mathcal{W}_c$  saturates to 0.5 in the strong coupling and up to the onset of the USC regime. Still increasing  $\eta$ , the ratio  $\mathcal{W}_c/\mathcal{W}_q$  then decreases dramatically: the Purcell effect is reversed. A similar behavior has been predicted in a polariton system arising from the interaction of photons in a multimode cavity with collective electronic (bosonic) excitations [52], and experimentally confirmed in three-dimensional crystals of plasmonic nanoparticles interacting with light in the DSC regime [54].

It is interesting to explore the impact on the photon emission rate of not taking into account the proper transformation of the photon operators, when adopting the dipole gauge ( $\tilde{\mathcal{W}}_c'$ ).

The dot-dashed black curves in Fig. 1 displays such a wrong result. The differences with respect to the correct results  $\mathcal{W}_c$  become evident at the onset of the USC regime ( $\eta \approx 0.1$ ). In the DSC regime, the impact of this mistake becomes very relevant:  $\mathcal{W}_c'$  does not go to zero and becomes orders of magnitudes larger than the qubit emission rate  $\mathcal{W}_q$ .

In Fig. 3(a) it is also displayed an approximate analytical derivation of the ratio  $\mathcal{W}_c/\mathcal{W}_q$ . When the coupling rate  $\eta$  is strong enough to split sufficiently the two lowest-energy excited levels (so that, at very low effective temperatures, only the system ground state and the first-excited level are populated) the higher energy levels can be neglected (effective dressed two-level system). For these values of  $\eta$ , the cavity and emission rates can be simplified to

$$\begin{aligned} \mathcal{W}_c &\simeq \frac{\omega_{\tilde{1}_-, \tilde{0}}^2}{\omega_c^2} |\langle \tilde{1}_- | (\hat{a} + \hat{a}^\dagger) | \tilde{0} \rangle|^2 \rho_{\tilde{1}_-, \tilde{1}_-}^{ss}, \\ \mathcal{W}_q &\simeq \frac{\omega_{\tilde{1}_-, \tilde{0}}^2}{\omega_q^2} |\langle \tilde{1}_- | \hat{\sigma}_x | \tilde{0} \rangle|^2 \rho_{\tilde{1}_-, \tilde{1}_-}^{ss}, \end{aligned} \quad (27)$$

where  $\rho^{ss}$  indicates the steady-state density operator. It is interesting to note that the ratio  $\mathcal{W}_c/\mathcal{W}_q$  in Eq. (27) is independent of the density matrix. This approximate value of the ratio (red-dashed curve), shown in Fig. 3(a), is able to reproduce accurately the numerically calculated values of  $\mathcal{W}_c/\mathcal{W}_q$  for  $\eta > 10^{-3}$ . In Fig. 3(b) it is shown the square modules of the transition matrix elements  $|\langle \tilde{1}_- | (\hat{a} + \hat{a}^\dagger) | \tilde{0} \rangle|^2$  and  $|\langle \tilde{1}_- | \hat{\sigma}_x | \tilde{0} \rangle|^2$  as a function of the normalized coupling  $\eta$ . In the high- $\eta$  limit, the first one goes to 0 and the second to 1.

In summary, the scenario in the high- $\eta$  and low-qubit-temperature limit is the following: the qubit spontaneous emission rate  $\mathcal{W}_q$  goes to zero because  $\Gamma_{\tilde{1}_-, \tilde{0}}^q \rightarrow 0$  (qubit decoupling from its reservoir) and the cavity emission rate  $\mathcal{W}_c$  goes to zero even more rapidly (at increasing  $\eta$ ) because  $|\langle \tilde{1}_- | (\hat{a} + \hat{a}^\dagger) | \tilde{0} \rangle|^2 \rightarrow 0$  and  $|\langle \tilde{1}_- | \hat{\sigma}_x | \tilde{0} \rangle|^2 \rightarrow 1$  (light-matter decoupling).

## 2. Cavity and qubit emission spectra

Figure 4 shows the cavity and qubit emission spectra under incoherent weak excitation of the qubit ( $T_q = 5 \times 10^{-2}$ ) in the weak and strong-coupling regimes ( $2 \times 10^{-5} < \eta < 4 \times 10^{-2}$ ). All the presented spectra are individually normalized, so that, in each spectral image the highest value is set to one. The transition from the weak (a single spectral line) to the strong (split lines) is clearly visible in the upper panel of Fig. 4. The two lines correspond to the transitions  $|\tilde{1}_\pm\rangle \rightarrow |\tilde{0}\rangle$  indicated as  $(\tilde{1}_-, \tilde{0})$  and  $(\tilde{1}_+, \tilde{0})$  in Fig. 2. In the weak-coupling regime, the emission line becomes brighter at increasing values of  $\eta$ . In the strong-coupling regime, when the two lines are sufficiently split, an asymmetry in their relative intensity can be observed. This is a direct consequence of the higher population of the lower-energy excited state  $|\tilde{1}_-\rangle$  with respect to the higher-energy state  $|\tilde{1}_+\rangle$  at  $T_q = 5 \times 10^{-2}$ . This behavior cannot be reproduced using the standard quantum-optics master equation where the reservoir occupations are calculated at the bare (in the absence of light-matter interaction) transition frequencies (see Sec. D). Across the transition from the weak to the strong-coupling regime,

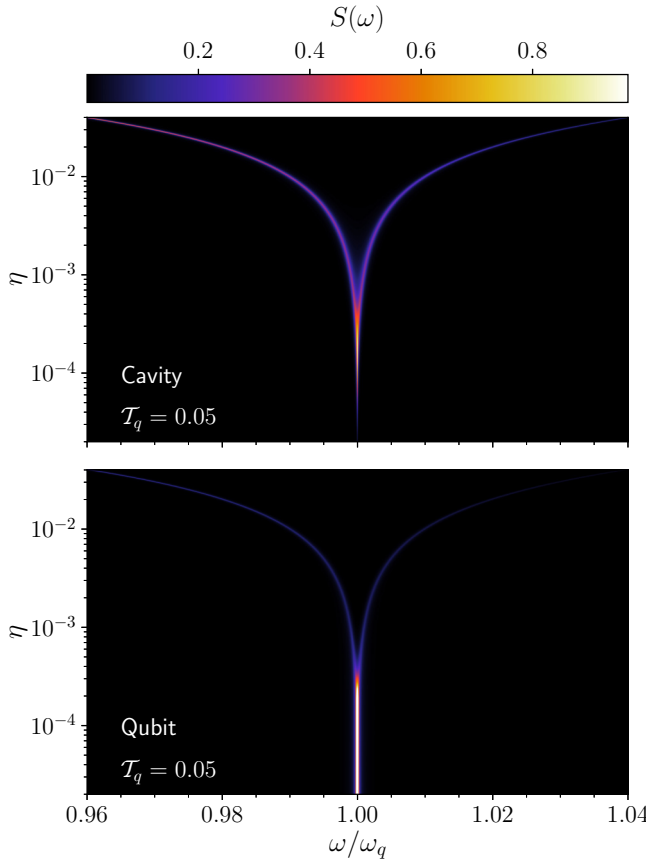


FIG. 4. Cavity  $S_c(\omega)$  and qubit  $S_q(\omega)$  emission spectra in the weak and strong-coupling regimes, calculated for  $2 \times 10^{-5} < \eta < 4 \times 10^{-2}$ , and for  $\Delta = 0$ . The spectra have been obtained under weak incoherent excitation of the qubit. We used an effective qubit temperature  $T_q = 5 \times 10^{-2}$ . The spectra have been normalized, so that the highest peak in each density plot is set at 1.

the qubit emission (lower panel) decreases approximately by an order of magnitude (see also Fig. 1).

Figure 5 displays logarithmic cavity emission spectra  $\ln[S_c(\omega)]$  as a function of the normalized coupling strength  $\eta$ , calculated for four different temperatures, showing the evolution of the emission spectra from the strong to the DSC regimes. In contrast with the case of light-matter systems described by a harmonic Hamiltonian (see, e.g., Ref. [84]), in the present highly anharmonic case, the spectra become very rich, if the system is adequately excited. On this scale, the weak-coupling regime (already shown in Fig. 4) is confined to a negligible portion of the y axis and is not visible. At very low temperature ( $T_q = 5 \times 10^{-2}$ ), only two spectral lines emerge, corresponding to the transitions  $(\tilde{1}_\pm, \tilde{0})$  [see Fig. 2(b)].

Notice that the transition  $(\tilde{1}_+, \tilde{1}_-)$  is forbidden owing to parity symmetry [3]. As expected, at such a low temperature, the emission from the lowest excited level at frequency  $\omega_{\tilde{1}_+, \tilde{0}}$  dominates. Moreover, the line at  $\omega_{\tilde{1}_+, \tilde{0}}$  is visible only for  $\eta \lesssim 0.3$ . When  $\eta$  increases (up to  $\eta \simeq 1$ ), the intensity of the line  $\omega_{\tilde{1}_+, \tilde{0}}$  increases, due to the lowering of the ratio  $\omega_{\tilde{1}_+, \tilde{0}}/(\omega_q T_q)$  which causes an increase of the excited-state population  $\rho_{\tilde{1}_+, \tilde{1}_-}$ . Then, for  $\eta \gtrsim 1$ , the population starts decreasing as a consequence of both light-matter and qubit-

reservoir decoupling. This behavior is in agreement with the corresponding emission rate in Fig. 1(b).

At  $\mathcal{T} = 0.1$ , the transition at frequency  $\omega_{\tilde{1}_+, \tilde{0}}$  becomes visible for all the values of  $\eta$  in the plot, although in the DSC regime, it tends to dissolve, owing to the qubit-reservoir decoupling which prevents the excitation of the excited energy levels. We also notice that a new resonance line at frequency  $\omega_{\tilde{2}_-, \tilde{1}_-}$  appears [see Fig. 2(b)].

When further increasing the temperature ( $\mathcal{T}_q = 0.2$ ), additional energy levels get populated and additional spectral lines appear. Most of these correspond to transitions indicated in Fig. 2(b). In the low-frequency range, in addition to the transition  $(\tilde{1}_-, \tilde{0})$ , a new spectral line at  $|\omega_{\tilde{2}_-, \tilde{1}_-}|$  appears. This transition is forbidden in the JCM, since  $\langle 1_+ | (\hat{a} + \hat{a}^\dagger) | 2_- \rangle = 0$ , at  $\Delta = 0$ . The crossing between the energy levels  $\omega_{\tilde{2}_-}$  and  $\omega_{\tilde{1}_-}$ , occurring at  $\eta \approx \bar{\eta} = 0.43$ , manifests as a low spectral line approaching  $\omega = 0$  as  $\eta \rightarrow \bar{\eta}$ , and then (after the crossing), moving away from  $\omega = 0$ . At higher frequencies ( $\omega/\omega_q \approx 1$ ), other two crossing spectral lines become clearly visible. As shown in Fig. 2(b), they correspond to the transitions  $(\tilde{2}_+, \tilde{1}_+)$  and  $(\tilde{3}_-, \tilde{1}_-)$ , both forbidden in the JCM at zero detuning. Still at higher frequencies, other two lines are observable for  $\eta \gtrsim 0.4$ : they correspond to the transitions  $(\tilde{2}_+, \tilde{1}_-)$  and  $(\tilde{3}_-, \tilde{0})$  [see Fig. 2(b)]. In the latter, the involved states differ by a number of excitations  $\Delta\tilde{n} = 3$ . This transition is enabled by the presence of the counter-rotating terms in the QRM (10) and represents a clear example of USC physics [3], beyond the JCM. The spectra obtained at  $\mathcal{T}_q = 0.5$  display still richer structures with the appearance of additional lines originated by higher energy levels that get populated at this effective temperature.

The qubit emission spectra  $S_q(\omega)$  calculated at  $\mathcal{T}_q = 0.2$  are shown in Fig. 6. As expected, emission lines corresponding to those observed for  $S_c(\omega)$  at the same temperature are shown. However, several differences emerge. In particular the spectral lines as a function of  $\eta$  display different relative intensities. For example, (i) two of the four lines around  $\omega \approx 1$  in  $S_c(\omega)$  are not visible in  $S_q(\omega)$ ; (ii) the line corresponding to the transition  $(\tilde{2}_-, \tilde{1}_+)$  is more visible at small values of  $\eta$ ; (iii) at increasing values of  $\eta$ ,  $S_q(\omega)$ , in contrast with  $S_c(\omega)$ , exhibits an increasing background emission and a faster dissolving of the spectral lines at increasing values of  $\eta$ . All these differences originate from the different matrix elements in Eq. (26) [ $\langle j | (\hat{a} + \hat{a}^\dagger) | k \rangle$  and  $\langle j | \hat{\sigma}_x | k \rangle$ ] entering  $S_c(\omega)$  and  $S_q(\omega)$ , respectively. In particular, the most peculiar feature (iii) is a direct consequence of the fact that, for  $\eta \gtrsim 1.5$ , the matrix elements  $\langle j | \hat{\sigma}_x | k \rangle \rightarrow 0$  for transitions with  $\omega_{kj}$  which are significantly different from zero. Therefore, for large values of  $\eta$ , the qubit spectra  $S_q(\omega)$  [see Eq. (25)] can be approximated by a Lorentzian lineshape (times  $\omega^2$ ) centered at  $\omega \approx 0$ :

$$S_q(\omega) \propto \omega^2 \frac{\gamma^2}{\omega^2 + \gamma^2}, \quad (28)$$

which, for  $\omega \gg \gamma$ , provides an almost constant background. Such behavior can be clearly observed in Fig. 7(h). Notice that this high-frequency behavior can be an artifact originating from the assumption in Eq. (25) and from the absence of any cutoff mechanism. Of course, a realistic behavior in a so wide spectral range should include the specific frequency

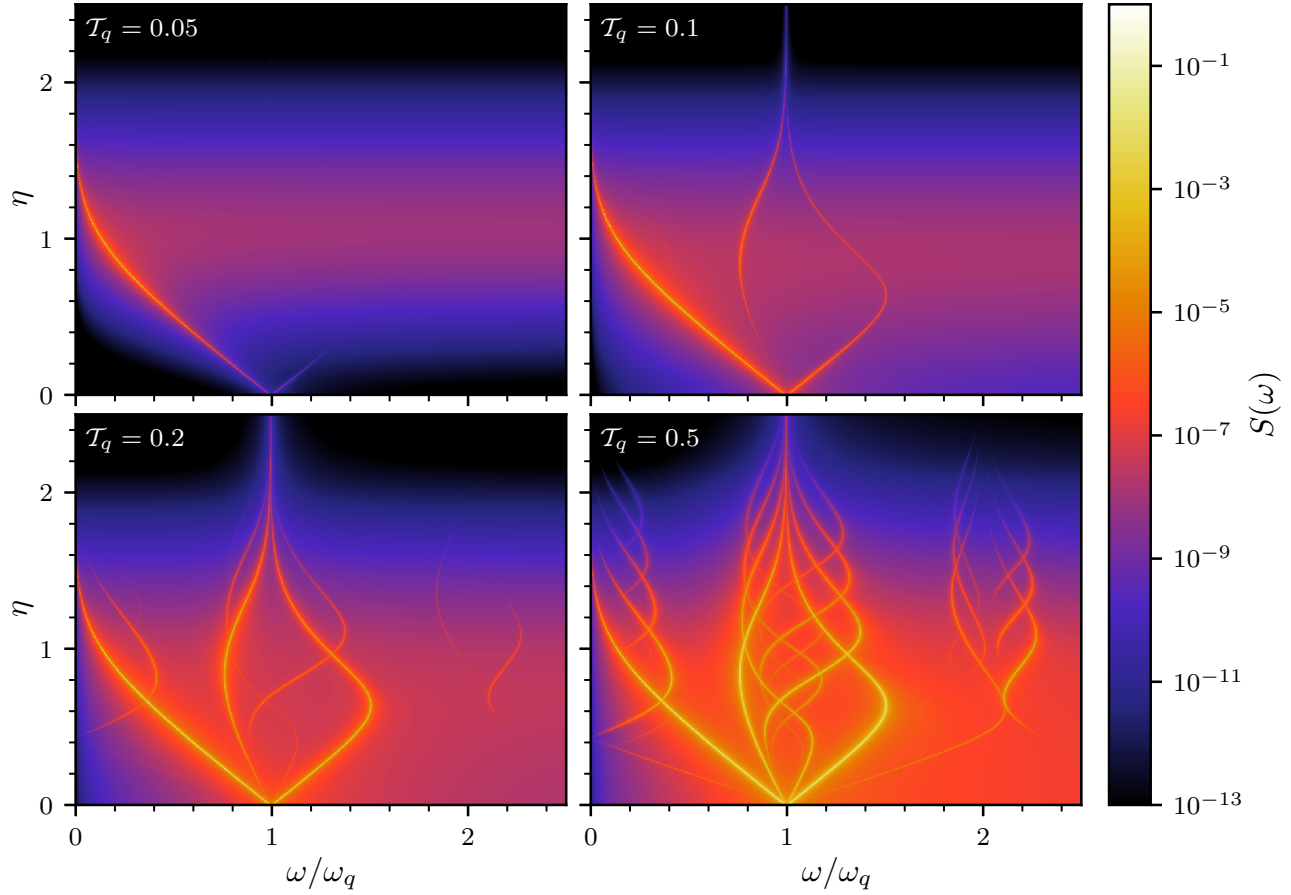


FIG. 5. Logarithmic two-dimensional plots of cavity emission spectra  $S_c(\omega)$  for values of  $\eta$  reaching the USC and DSC regimes obtained using four different effective qubit temperatures  $T_q$ , and  $\Delta = 0$ . The spectra have been normalized so that the highest peak in each density plot is set at 1. Increasing the temperature, additional lines originating from transitions involving higher energy levels appear. Most of the emission lines correspond to transition energies shown in Fig. 2.

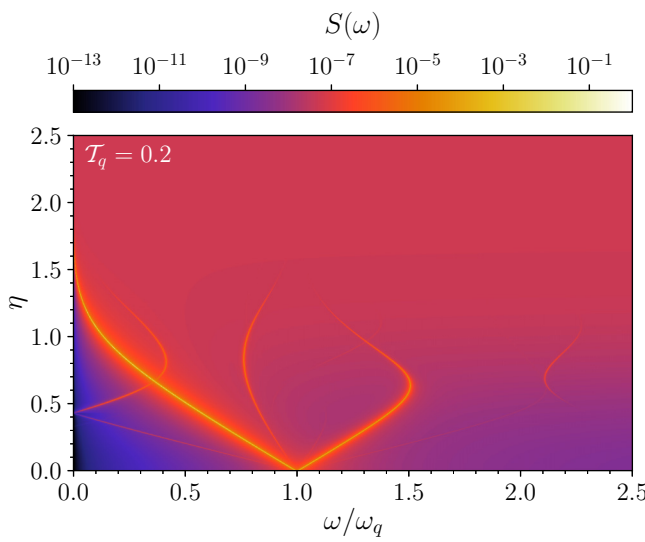


FIG. 6. Logarithmic two-dimensional plots of qubit emission spectra  $S_q(\omega)$  for values of  $\eta$  reaching the USC and DSC regimes, obtained at  $T_q = 0.2$  and  $\Delta = 0$ . The spectra have been normalized so that the highest peak is set at 1. The visible lines correspond to transition energies shown in Fig. 2. The origin of the flat (red) signal background for  $\eta > 1.5$  is explained in the text [see Eq. (28)].

dispersion of the resonator materials, which in general is system dependent and goes beyond the present general treatment.

Figure 7 displays cavity and qubit emission spectra  $S_{c(q)}(\omega)$  for four values of the normalized coupling strength  $\eta$ , calculated at  $T_q = 0.5$ . The plots on the left correspond to horizontal line cuts of the bottom-right density plot in Fig. 5. For a more accurate comparison, the spectra in Fig. 7 are reported all on the same  $x$  and  $y$  scale and have been normalized by the same amount, so that the highest peak in the figure is set to 1. Each spectral line in Fig. 7 originates from a specific transition between pairs of energy levels of the QRM [see Fig. 2].

These spectra show more in detail several features already present in the density plots. In particular, the six peaks in Figs. 7(a) and 7(b) originate from the following transitions (from the left):  $(\tilde{2}_-, \tilde{1}_+)$ ,  $(\tilde{1}_-, \tilde{0})$ ,  $(\tilde{2}_-, \tilde{1}_-)$ ,  $(\tilde{2}_+, \tilde{1}_+)$ ,  $(\tilde{1}_+, \tilde{0})$ ,  $(\tilde{2}_+, \tilde{1}_-)$ . In Figs. 7(e) and 7(f) at  $\eta = 1$ , the highest peak for both the cavity and qubit spectrum is the one at the lowest frequency and corresponds to the transition  $(\tilde{1}_-, \tilde{0})$ . Moreover, at this coupling strength, higher-energy peaks around  $\omega/\omega_q \approx 2$ , due to transitions from states differing by two excitations  $\Delta\tilde{n} = 2$ , can be observed. At  $\eta = 2$ , well in the DSC regime, the intensity of the emission spectra decreases. Now  $S_c(\omega)$  shows bunches of peaks centered at  $\omega \approx 0, 1, 2$ ,

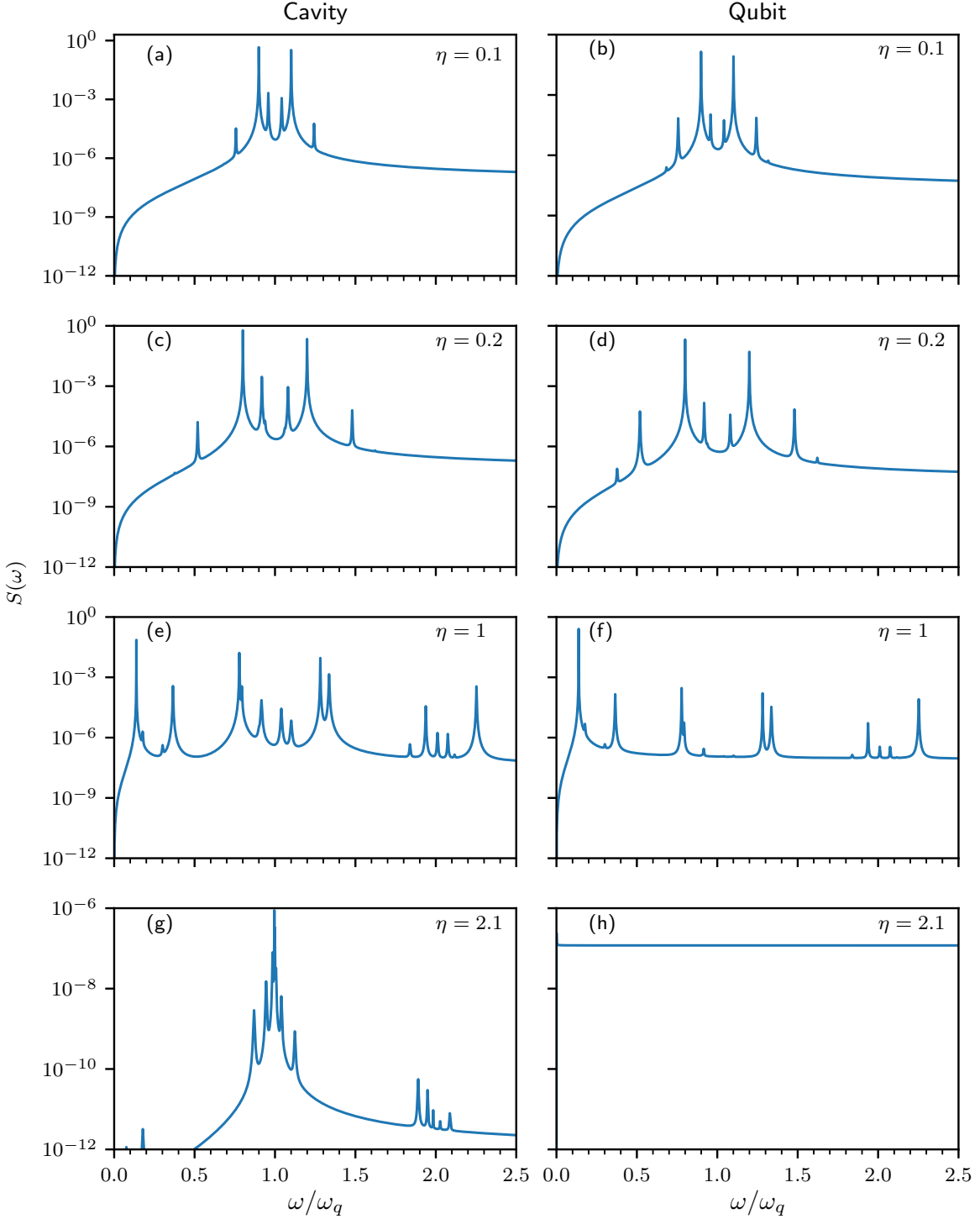


FIG. 7. Cavity  $S_c(\omega)$  and qubit  $S_q(\omega)$  emission spectra (logarithmic), obtained at four different values of  $\eta$ , increasing from the top to the bottom (detuning  $\Delta = 0$ ). The cavity spectra are on the left, while the qubit ones on the right side. We used an effective temperature for the qubit reservoir  $T_q = 0.5$ . The cavity and qubit spectra have been normalized to the highest peak which appears in panels (c) and (d), respectively. The plots show the evolution of the cavity and qubit emission spectra when increasing the normalized coupling strength  $\eta$ . Panel (h) reveals the flat background appearing in the qubit emission spectra in the DSC regime.

due to the tendency of the energy levels of the system towards a harmonic spectrum in the large- $\eta$  limit (see Fig. 2). In Fig. 7(h) is displayed a very different behavior consisting of the constant emission background explained above [see Eq. (28)].

### B. Cavity-qubit interaction in the presence of detuning

We now present numerically calculated emission rates and spectra obtained in the case of significant qubit-cavity detuning  $\Delta \equiv (\omega_c - \omega_q)/\omega_q$ , in normalized units. In particular,

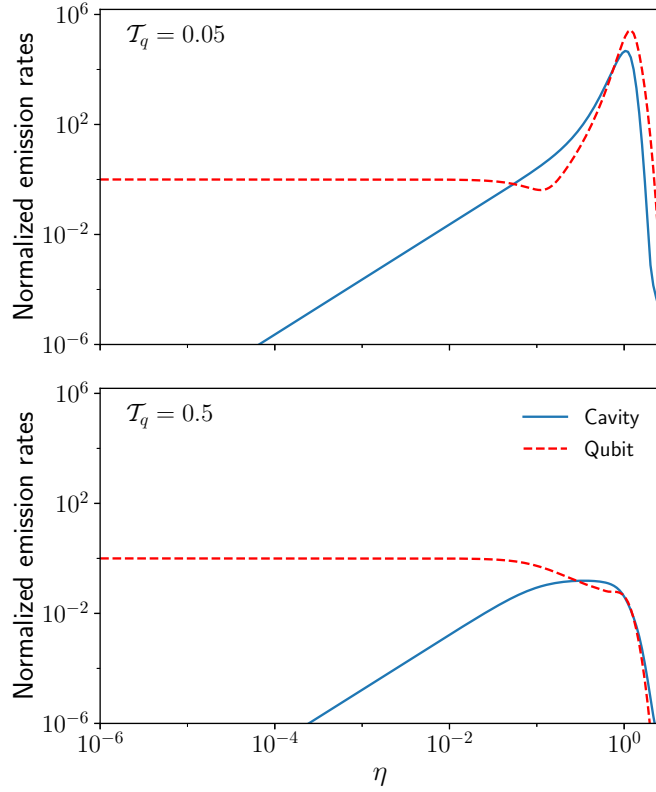


FIG. 8. Cavity and qubit emission rates (normalized with respect to the qubit emission rate  $W_q^0$  calculated for  $\eta = 0$ )  $\mathcal{W}_c = W_c/W_q^0$  (blue continuous curve), and  $\mathcal{W}_q = W_q/W_q^0$  (red dashed) versus the light-matter normalized coupling strength  $\eta$ . We used  $\Delta = -0.3$ , corresponding to  $\omega_c/\omega_q = 0.7$ . The upper panel has been obtained for  $T_q = 5 \times 10^{-2}$ , the lower one for  $T_q = 5 \times 10^{-1}$ .

here we consider the cases of  $\Delta = -0.3$ , while in Appendix C we analyze the positive-detuning case.

We start from a detuning value of  $\Delta = -0.3$ . Figure 8 shows the normalized cavity and qubit emission rates, obtained with the same parameters used to calculate the results in Fig. 1, except the finite detuning. At very low effective temperature  $T_q = 5 \times 10^{-2}$ , and at low coupling strengths, the cavity emission rate  $\mathcal{W}_c$  increases linearly (on this log-log scale) as the zero-detuning case, but it is some orders of magnitude smaller. As expected, the large detuning significantly reduces the energy transfer from the qubit to the cavity for  $\omega_q\eta \ll \Delta$ . However, the cavity emission rate becomes of the same order of magnitude of the qubit emission at  $\eta \approx 0.05$ , when  $\omega_q\eta < \Delta$ .

Moreover, the plateau in the strong-coupling regime is no longer present, hence the standard Purcell behavior continues in the USC regime. In the  $\eta$  region  $5 \times 10^{-2} \lesssim \eta \lesssim 0.5$ , the cavity emission rate exceeds that of the qubit ( $\mathcal{W}_c > \mathcal{W}_q$ ). The qubit emission rate is almost constant from the weak-coupling regime to the onset of the USC, where it reaches values which are more than five orders of magnitude greater than the qubit emission rate at zero coupling  $W_q^0$ . As in the zero-detuning case, the strong enhancement of both the emission rates in the USC regime and at low effective temperature originates from the decrease of the transition frequency  $\omega_{\tilde{1}_{-},0}$ , and, as

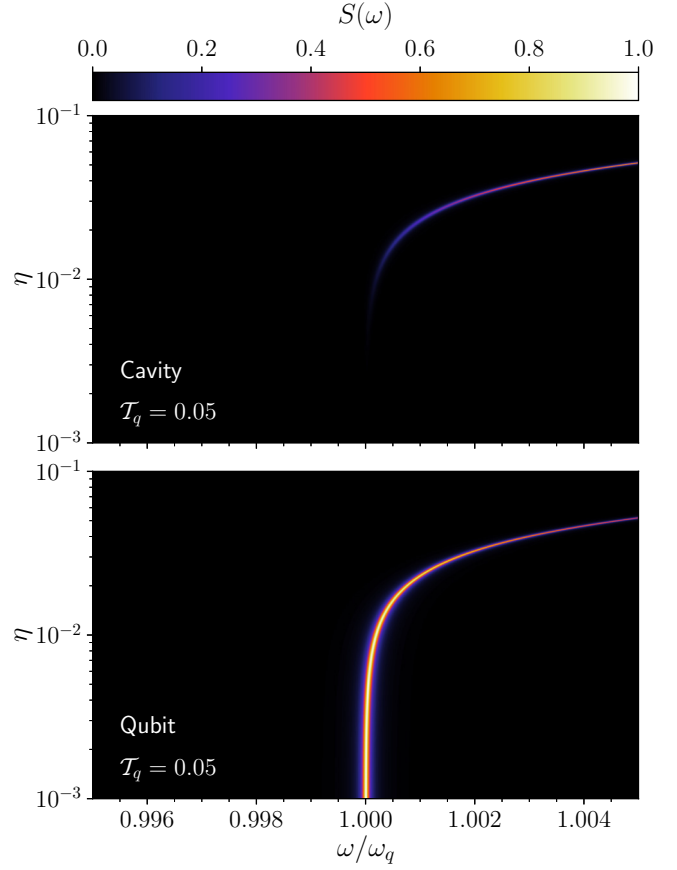


FIG. 9. Cavity  $S_c(\omega)$  and qubit  $S_q(\omega)$  emission spectra in the weak and strong-coupling regime, calculated for  $10^{-3} < \eta < 10^{-1}$ , and for  $\Delta = -0.3$  ( $\omega_c/\omega_q = 0.7$ ). The spectra have been obtained under weak incoherent excitation of the qubit. We used an effective qubit temperature  $T_q = 5 \times 10^{-2}$ . The spectra have been normalized, so that the highest peak in each density plot is set at 1.

stated above, it is not present at higher effective temperatures. Moreover, beyond the DSC regime onset ( $\eta > 1$ ), both  $\mathcal{W}_c$  and  $\mathcal{W}_q$  decrease rapidly because of the light-matter and qubit-reservoir decoupling.

Figure 9 shows the low-temperature ( $T_q = 5 \times 10^{-2}$ ) cavity and qubit emission spectra in the weak and strong-coupling regimes ( $10^{-5} \leq \eta \leq 3 \times 10^{-2}$ ), in analogy with the zero-detuning case in Fig. 4. As can be seen in Fig. 10, in the weak-coupling regime  $\omega_{\tilde{1}_{-},0} \approx \omega_c$  and  $\omega_{\tilde{1}_{+},0} \approx \omega_q$ . Moreover, at low values of the coupling strength and at low incoherent excitation rates (low temperature), the cavity cannot emit at the qubit frequency  $\omega_q$ , and the qubit cannot emit at  $\omega_c$ . Thus, Fig. 9 shows only the  $(\tilde{1}_{+}, 0)$  transition, while the  $(\tilde{1}_{-}, 0)$  transition is absent. Another difference between Fig. 9 and Fig. 4 is the intensity of the Purcell effect, which is much more effective in the zero-detuned case. Here the cavity starts to emit at  $\eta \approx 10^{-2}$ , a value which is three orders of magnitude greater than the zero-detuning case.

Figure 11 shows a logarithmic plot of the cavity emission spectra  $S_c(\omega)$  as a function of the normalized coupling strength  $\eta$  ranging from the strong to the DSC regimes. As in the zero-detuning case, at very low effective temperature ( $T_q = 5 \times 10^{-2}$ ), the transition  $(\tilde{1}_{-}, 0)$  is the brightest, while

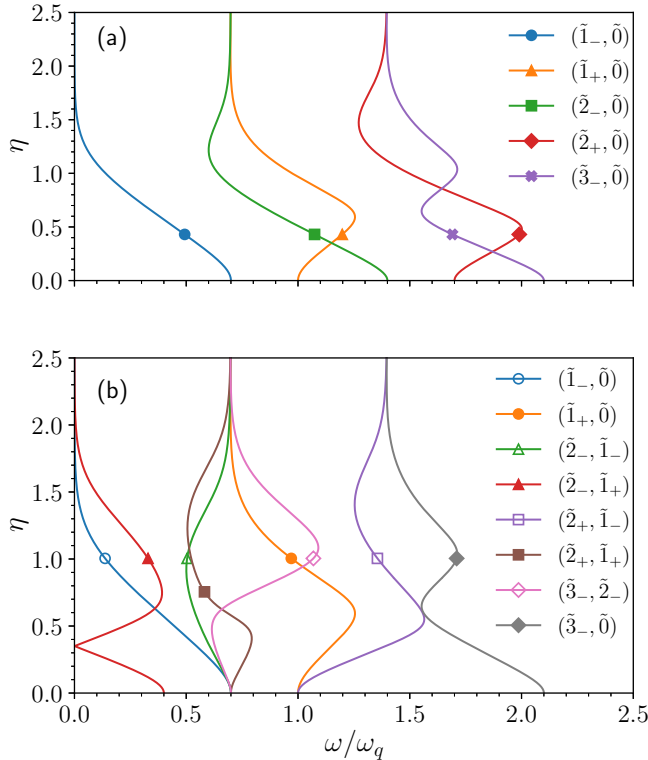


FIG. 10. Normalized energy levels and transition energies versus  $\eta$  for  $\Delta = -0.3$  ( $\omega_c/\omega_q = 0.7$ ). (a) Lowest normalized energy levels (with the ground-state energy as reference)  $(\omega_{\tilde{j}\pm} - \omega_{\tilde{0}})/\omega_q$  of the QRM. (b) Normalized parity-allowed transition energies  $|\omega_{\tilde{j}\pm} - \omega_{\tilde{k}\pm}|/\omega_q$  for the lowest eigenstates of the QRM.

the atom-like transition  $(\tilde{1}_+, \tilde{0})$  is visible only for  $\eta \lesssim 0.4$ . We also notice that the line at frequency  $\omega_{\tilde{2}_-, \tilde{1}_-}$  becomes slightly visible only for  $0.7 \lesssim \eta \lesssim 1.7$ .

At  $T_q = 0.5$ , additional energy levels get populated and additional spectral lines appear. As in the zero-detuning case, most of these transitions can be found in Fig. 10(b). The line at frequency  $\omega_{\tilde{2}_-, \tilde{1}_+}$  becomes sufficiently intense only for  $\eta \gtrsim 0.35$ , which is when the  $(\tilde{1}_+, \tilde{0})$  frequency transition becomes greater than  $(\tilde{2}_-, \tilde{0})$ . We also observe that, at the higher effective temperature and at low coupling strengths (but with  $\eta \gtrsim 0.05$ ), the cavity can also emit significantly at the qubit frequency  $\omega_q$ . It is worth noting that at very high coupling strengths, all the spectral lines tend to be at frequencies which are multiple integer of the cavity frequency  $\omega_c$ .

Figure 12 displays the logarithmic qubit emission spectra  $S_q(\omega)$ , which present features similar to those in the cavity emission spectrum but with a background emission above the onset of the deep USC regime.

#### IV. CONCLUSIONS

We have investigated how the QRM emits light under incoherent excitation of the two-level atom, considering coupling strengths ranging from the weak coupling to the USC and DSC regimes. We analyzed both the cavity and the qubit emission, for both the resonant and detuned cases, considering different effective qubit temperatures. In particular, by using a

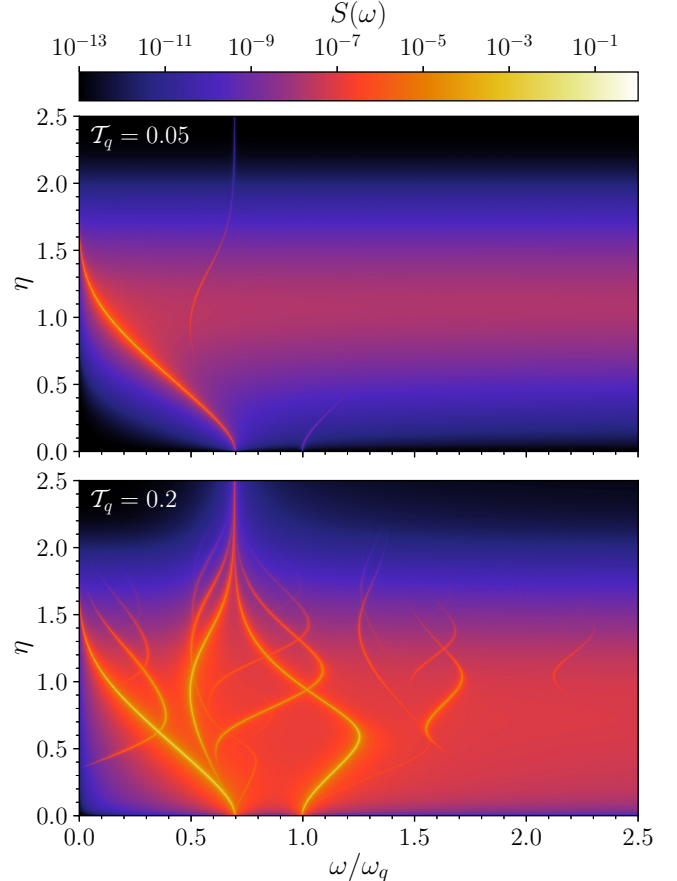


FIG. 11. Cavity emission spectra  $S_c(\omega)$  on logarithmic scale for values of  $\eta$  reaching the USC and DSC regimes, obtained for two different effective qubit temperatures  $T_q = 0.05, 0.2$ . We used  $\Delta = -0.3$  ( $\omega_c/\omega_q = 0.7$ ). The spectra have been normalized, so that the highest peak in each density plot is set at 1. Increasing the temperature, additional lines originating from transitions involving higher energy levels appear, where the majority of these correspond to transition energies shown in Fig. 10.

GME approach, we were able to calculate numerically cavity and qubit emission rates and spectra versus the normalized light-matter coupling strength and for different incoherent qubit excitation strengths (effective temperature). Following the work in Ref. [63], the obtained results are gauge independent. The theoretical framework allows us to investigate the light-matter decoupling and the fate of the Purcell effect in the QRM when the normalized coupling strength  $\eta$  is significantly larger than one. In this case, we found that the cavity and qubit emission rates are affected both by light-matter decoupling and qubit-reservoir decoupling.

Reaching the USC and DSC regimes with individual quantum emitters, whose interaction with light is implemented via the minimal-coupling replacement, is currently very difficult, although progress is being made, especially with plasmonic cavity systems [54]. However, this theoretical framework can be easily generalized to include  $N$  qubits (Dicke model) [60]. Moreover, coupling strengths ranging from the weak to the DSC regime can be achieved with individual qubits using superconducting circuits (see, e.g., Refs. [31,85]). In this case,

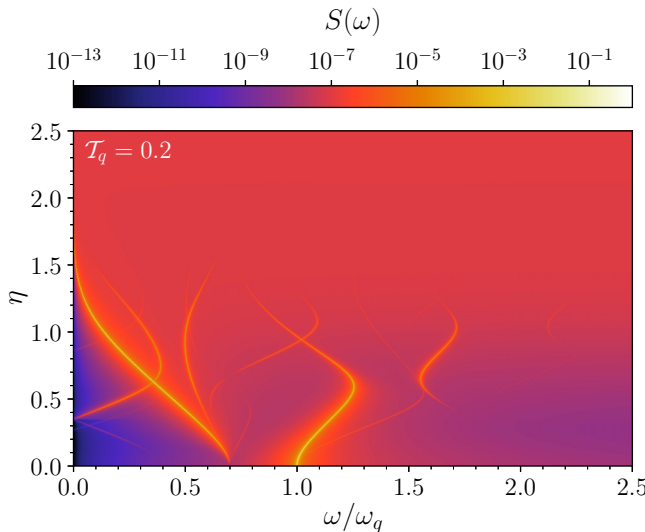


FIG. 12. Logarithmic qubit emission spectra  $S_q(\omega)$  for values of  $\eta$  reaching the USC and DSC regimes, obtained at  $T_q = 0.2$ . We used  $\Delta = -0.3$ . The spectra have been normalized so that the highest peak is set at 1. The visible lines correspond to transition energies shown in Fig. 2. The origin of the flat (red) signal background for  $\eta > 1.5$  is explained in the text [see Eq. (28)].

however, the light-matter interaction is not described by the minimal-coupling replacement and specific calculations for these systems would have to be carried out, where the general approach described here and these results can provide a precise guide.

## ACKNOWLEDGMENTS

F.N. is supported in part by Nippon Telegraph and Telephone Corporation (NTT) Research, the Japan Science and Technology Agency (JST) [via the Quantum Leap Flagship Program (Q-LEAP), and the Moonshot R&D Grant Number JPMJMS2061, the Japan Society for the Promotion of Science (JSPS) [via the Grants-in-Aid for Scientific Research (KAKENHI) Grant No. JP20H00134, the Army Research Office (ARO) (Grant No. W911NF-18-1-0358), the Asian Office of Aerospace Research and Development (AOARD) (via Grant No. FA2386-20-1-4069), and the Foundational Questions Institute Fund (FQXi) via Grant No. FQXi-IAF19-06. S.S. acknowledges the Army Research Office (ARO) (Grant No. W911NF-19-1-0065). S.H. thanks the Natural Sciences and Engineering Research Council of Canada, the Canadian Foundation for Innovation, the National Research Council of Canada, and Queen's University.

## APPENDIX A: CAVITY- AND QUBIT-BATH INTERACTIONS FROM THE GAUGE PRINCIPLE

A simple and widely adopted way to model the interaction of a quantum system with its environment consists in writing the interaction Hamiltonian in a quadratic form involving the product of system- and bath-degrees of freedom:

$$\hat{H}_I = \sum_k \lambda_k \hat{S} \hat{B}_k, \quad (\text{A1})$$

where the coefficients  $\lambda_k$  represent the coupling strengths (assumed real, one for any bath-degree of freedom), while  $\hat{S}$  and  $\hat{B}_k$  are Hermitian system- and bath-operators. The specific values of the coupling strengths and the choice of the system and bath operators in Eq. (A1) is model dependent. In the next sections, we present arguments to guide and to make these choices consistent (taking care of gauge issues). Specifically, we present a consistent derivation for the QRM, describing the interaction of the cavity mode and the qubit with their respective baths.

The approach followed here is close to that recently developed in Ref. [63] and gives rise to analogous results. The only difference is that here we introduce the interaction of the photonic and matter components with their reservoirs by invoking the gauge principle. This approach provides a rather fundamental model of systems-baths interactions and connects more with quantum field theory.

### 1. Cavity-Bath Interaction in the Coulomb and Dipole Gauges

Here, we introduce the cavity-bath coupling by regarding the environment as collective bosonic excitations of matter so that we can introduce such interaction by invoking the fundamental gauge principle, which determines the form of light-matter coupling.

#### a. Cavity-bath interaction in the Coulomb gauge

As a consequence of the gauge principle (minimal-coupling replacement), in the Coulomb gauge, the only degrees of freedom of the electromagnetic field interacting with matter are the field coordinates  $\hat{x}$ , which can be expressed as  $\hat{x} = \hat{a} + \hat{a}^\dagger$ . This fact not only leads to the useful relation in Eq. (6), but it also allows us to obtain a Thomas-Reiche-Kuhn (TRK) sum rule for the electromagnetic field [69].

Usually, input-output frameworks, which are used to model the interaction of cavity modes with the external modes, adopt as bath operators a continuum of bosonic electromagnetic modes, rather than a collection of bosonic matter excitations. However, the field-bath coupling ultimately originates from the interaction of the cavity electromagnetic field with matter (e.g., cavity mirrors). Due to this fact, even if such matter degrees of freedom can be adiabatically eliminated, it is reasonable to require that the general relationship (6) and the TRK sum rule remain valid. To ensure this, it is sufficient to start from the free bosonic Hamiltonian for the bath,  $\hat{H}_b = \sum_k \omega_k \hat{b}_k^\dagger \hat{b}_k$ , and to apply the *generalized minimal-coupling replacement*, which corresponds to transforming each matter operator of the bath by a suitable unitary transformation (see Ref. [60]):

$$\hat{b}_k \rightarrow \hat{U}_{cb} \hat{b}_k \hat{U}_{cb}^\dagger = \hat{b}_k - i\eta_k^c (\hat{a} + \hat{a}^\dagger), \quad (\text{A2})$$

where

$$\hat{U}_{cb} = \exp \left[ i(\hat{a} + \hat{a}^\dagger) \sum_k \eta_k^c (\hat{b}_k + \hat{b}_k^\dagger) \right]. \quad (\text{A3})$$

Assuming a coupling constant (effective charge  $q$ ) independent on the matter mode  $k$ ,  $\hat{U}_{cb}$  can be written as

$$\hat{U}_{cb} = \exp[iq\hat{x} \hat{Q}_b], \quad (\text{A4})$$

where the coordinate of the reservoir field reads

$$\hat{Q}_b = \sum_k \frac{\alpha}{\sqrt{\omega_k}} (\hat{b}_k + \hat{b}_k^\dagger). \quad (\text{A5})$$

Here  $\alpha$  is a constant. The resulting adimensional coupling in Eq. (A3) can be expressed as

$$\eta_k^c = q\alpha/\sqrt{\omega_k}. \quad (\text{A6})$$

Of course, depending on the specific model, the effective charge can be frequency dependent, implying a different frequency dependence of  $\eta_k^c$  than that in Eq. (A6). By neglecting the diamagnetic term [of the second order  $\eta_k^c(\omega_k)$ ], we obtain the interaction Hamiltonian for the cavity field and the reservoir

$$\hat{H}_{cb} = i(\hat{a} + \hat{a}^\dagger) \sum_k \omega_k \eta_k^c (\hat{b}_k - \hat{b}_k^\dagger). \quad (\text{A7})$$

A comparison between Eq. (A1) and Eq. (A7) clearly shows that  $\hat{S} = (\hat{a} + \hat{a}^\dagger)$  and  $\hat{B}_k = i\omega_k(\hat{b}_k - \hat{b}_k^\dagger)$ .

Equation (A7) represents a consistent starting point to study the interaction of the cavity mode with its bath. To derive the GME (see Appendix B), it is useful to expand the cavity-field coordinate in the dressed basis,

$$\hat{H}_{cb} = i \sum_{l,m} x_{lm} \hat{P}_{lm} \sum_k \omega_k \eta_k^c (\hat{b}_k - \hat{b}_k^\dagger), \quad (\text{A8})$$

where  $\hat{P}_{lm} = |l\rangle\langle m|$  are the transition operators and  $x_{lm} = \langle l|(\hat{a} + \hat{a}^\dagger)|m\rangle$  are the matrix elements for the cavity-field coordinate, with  $|l\rangle$  being the energy eigenstates of the Hamiltonian in the Coulomb gauge [Eq. (1) in Sec. II A]. In terms of cavity-photon operators with positive and negative frequencies [71], Eq. (A8) can be written as

$$\hat{H}_{cb} = i \sum_{l>m} (x_{lm} \hat{P}_{lm} + x_{ml}^* \hat{P}_{ml}) \sum_k \omega_k \eta_k^c (\hat{b}_k - \hat{b}_k^\dagger). \quad (\text{A9})$$

Note that  $\sum_{l>m} x_{lm} \hat{P}_{lm} = (\sum_{l<m} x_{ml}^* \hat{P}_{ml})^\dagger$ .

Since the system-bath interaction is assumed to be weak, it is reasonable to apply to Eq. (A9) the rotating wave approximation:

$$\hat{H}_{cb} = -i \sum_{l>m} x_{ml}^* \hat{P}_{ml} \sum_k \omega_k \eta_k^c \hat{b}_k^\dagger + \text{H.c.} \quad (\text{A10})$$

### b. Cavity-bath interaction in the dipole gauge

The cavity-bath interaction Hamiltonian in the dipole gauge could be obtained by simply performing the gauge transformation of the cavity operators in Eq. (A7):  $\hat{a} \rightarrow \hat{R}\hat{a}\hat{R}^\dagger = \hat{a} + i\eta^c \hat{\sigma}_x = \hat{a}'$ , where

$$\hat{R} = \exp[-i\eta(\hat{a} + \hat{a}^\dagger)\hat{\sigma}_x]. \quad (\text{A11})$$

Therefore,  $\hat{H}'_{cb}$  in the dipole gauge is equivalent to  $\hat{H}_{cb}$  in the Coulomb gauge, because  $\hat{x}' = \hat{R}\hat{x}\hat{R}^\dagger$ . In doing so, we are neglecting the action of the gauge transformation on the reservoir operators  $\hat{b}_k$  ( $\hat{b}_k^\dagger$ ), which is possible because, as shown in Ref. [59], gauge transformations affect significantly ladder operators only when the coupling is rather strong. Nevertheless, it remains interesting and instructive to derive directly the cavity-bath reservoir in the dipole gauge.

In general, for a light-matter system whose light component (in the absence of interaction) is described by the

Hamiltonian  $\hat{H}_{ph}$ , and matter component by  $\hat{H}_m$ , the total Hamiltonian (in the dipole approximation) in the presence of interaction can be obtained in the Coulomb gauge by applying a suitable unitary transformation  $\hat{U}$  to the matter Hamiltonian only:

$$\hat{H} = \hat{U}\hat{H}_m\hat{U}^\dagger + \hat{H}_{ph}. \quad (\text{A12})$$

The dipole gauge Hamiltonian is obtained from the above as

$$\hat{H}' = \hat{U}^\dagger \hat{H}_C \hat{U} = \hat{H}_m + \hat{U}^\dagger \hat{H}_{ph} \hat{U}, \quad (\text{A13})$$

which corresponds to applying a unitary transformation to the bare photonic Hamiltonian only: a sort of generalized minimal-coupling replacement for the photonic Hamiltonian. Of course, the dipole-gauge Hamiltonian can also be written using the unitary operator  $\hat{R} = \hat{U}^\dagger$ :

$$\hat{H}' = \hat{H}_m + \hat{R}\hat{H}_{ph}\hat{R}^\dagger. \quad (\text{A14})$$

In the present case, the generalized minimal-coupling replacement for a single-mode photonic system interacting with a two-level atom and with a bosonic matter field can be implemented by the following unitary operator:

$$\hat{R}_{cqg} = \exp \left\{ -i(\hat{a} + \hat{a}^\dagger) \left[ \eta \hat{\sigma}_x + \sum_k \eta_k^c (\hat{b}_k + \hat{b}_k^\dagger) \right] \right\}. \quad (\text{A15})$$

The dipole-gauge Hamiltonian for the system constituted by a cavity-mode interacting with a qubit and with a bosonic matter reservoir can be directly obtained applying the generalized gauge transformation [see Eq. (A15)] to the photon operators in the bare cavity Hamiltonian  $\hat{H}_{ph} = \omega_c \hat{a}^\dagger \hat{a}$ :

$$\hat{a} \rightarrow \hat{R}_{cqg} \hat{a} \hat{R}_{cqg}^\dagger = \hat{a} + i\eta \hat{\sigma}_x + i \sum_k \eta_k^c (\hat{b}_k + \hat{b}_k^\dagger). \quad (\text{A16})$$

The resulting cavity-bath interaction Hamiltonian in the dipole gauge becomes

$$\begin{aligned} \hat{H}'_{cb} = & -i\omega_c (\hat{a} - \hat{a}^\dagger + 2i\eta \hat{\sigma}_x) \sum_k \eta_k^c (\hat{b}_k + \hat{b}_k^\dagger) \\ & + \omega_c \left| \sum_k \eta_k^c (\hat{b}_k + \hat{b}_k^\dagger) \right|^2, \end{aligned} \quad (\text{A17})$$

which includes an effective interaction of the bath with the qubit, and a bath self-interaction term. The result in Eq. (A17) differs from what has been obtained above adopting a less rigorous approach ( $\hat{H}'_{cb} = \hat{H}_{cb}$ ). However, in Appendix B we show that the two approaches, after the Markov and Born approximations, give rise to the same dissipators in the master equation. Neglecting the bath self-interaction term [of second order  $\eta_k^2(\omega_k)$ ] and using the dipole-gauge photon operators in Eq. (13) (see Sec. II B), the cavity-bath interaction Hamiltonian in Eq. (A17) can be written as

$$\hat{H}'_{cb} = -i\omega_c (\hat{a}' - \hat{a}'^\dagger) \sum_k \eta_k^c (\hat{b}_k + \hat{b}_k^\dagger). \quad (\text{A18})$$

A comparison between Eq. (A1) and Eq. (A18) clearly shows that  $\hat{S} = -i\omega_c(\hat{a}' - \hat{a}'^\dagger)$  and  $\hat{B}_k = \hat{b}_k + \hat{b}_k^\dagger$ .

By expanding in Eq. (A18), the cavity operators in the dressed basis, we obtain

$$\hat{H}'_{cb} = -i\omega_c \sum_{m,l} p'_{lm} \hat{P}'_{lm} \sum_k \eta_k^c (\hat{b}_k + \hat{b}_k^\dagger), \quad (\text{A19})$$

where  $p'_{lm} = \langle l' | (\hat{a}' - \hat{a}'^\dagger) | m' \rangle$ , and  $\hat{P}'_{lm} = |l'\rangle\langle m'|$ , with  $|l'\rangle$  being the energy eigenstates of the Rabi Hamiltonian in dipole gauge [Eq. (10) in Sec. II B]. Looking at Eq. (19) in the main text, the above matrix element can also be written as  $p'_{lm} = \omega_{lm} x'_{lm} / \omega_c$ , with  $x'_{lm} = \langle l' | (\hat{a}' + \hat{a}'^\dagger) | m' \rangle$ . In terms of cavity-photon operators with positive and negative frequencies, we obtain

$$\hat{H}'_{cb} = -i \sum_{l>m} \omega_{lm} (x'_{lm} \hat{P}'_{lm} - x'^*_{ml} \hat{P}'_{ml}) \sum_k \eta_k^c (\hat{b}_k + \hat{b}_k^\dagger). \quad (\text{A20})$$

Note that  $\sum_{l>m} \omega_{lm} x'_{lm} \hat{P}'_{lm} = (\sum_{l>m} \omega_{ml} x'^*_{ml} \hat{P}'_{ml})^\dagger$ .

Finally, applying the RWA, Eq. (A20) becomes

$$\hat{H}'_{cb} = -i \sum_{m>l} \omega_{lm} x'_{lm} \hat{P}'_{lm} \sum_k \eta_k^c b_k^\dagger + \text{H.c.} \quad (\text{A21})$$

## 2. Modeling the qubit-bath interaction in the Coulomb and dipole gauges

Due to the fact that atoms interact with the electromagnetic field, here we model (as usual) the qubit-bath interaction considering the environment field as a free-space electromagnetic field described by a collection of harmonic oscillators. We indicate with  $\hat{c}_k$  and  $\hat{c}_k^\dagger$  the bosonic photon destruction and creation operators for the  $k$ th mode of the reservoir, so that the free reservoir Hamiltonian can be expressed as  $\hat{H}_c = \sum_k \omega_k \hat{c}_k^\dagger \hat{c}_k$ .

### a. Qubit-bath interaction in the Coulomb gauge

In the Coulomb gauge, in contrast with the field momenta, the matter momenta are modified by the light-matter interaction. In particular, the canonical momenta of the matter field differ from the kinetic momenta (see, e.g., Ref. [62]). Hence, this gauge is not the more convenient one to study the qubit properties.

The qubit-bath interaction Hamiltonian in the Coulomb gauge can be obtained by applying the generalized minimal-coupling replacement including, in addition to the qubit interaction with the cavity field, also the interaction with the environment. Specifically, the interaction of the qubit with the cavity and the bath fields can be directly obtained by applying to the qubit bare Hamiltonian  $\hat{H}_q = \omega_q \hat{\sigma}_z / 2$  a unitary transformation defined by the following unitary operator:

$$\hat{U}_{qb} = \exp \left\{ i\hat{\sigma}_x \left[ \eta(\hat{a} + \hat{a}^\dagger) + \sum_k \eta_k^q (\hat{c}_k + \hat{c}_k^\dagger) \right] \right\}. \quad (\text{A22})$$

Keeping only the linear terms in the qubit-bath coupling strength  $\eta_k^q$ , the resulting qubit-bath interaction Hamiltonian in the Coulomb gauge becomes (see Ref. [62])

$$\hat{H}_{qb} = \omega_q \hat{\Sigma}_y \sum_k \eta_k^q (\hat{c}_k + \hat{c}_k^\dagger), \quad (\text{A23})$$

where

$$\hat{\Sigma}_y \equiv \hat{\mathcal{R}}_{qb}^\dagger \hat{\sigma}_y \hat{\mathcal{R}}_{qb} = \hat{\sigma}_y \cos[2\eta(\hat{a} + \hat{a}^\dagger)] - \hat{\sigma}_z \sin[2\eta(\hat{a} + \hat{a}^\dagger)] \quad (\text{A24})$$

is the Pauli  $y$  operator in the dipole gauge, transformed in the Coulomb gauge, and  $\hat{\mathcal{R}}_{qb} = \hat{\mathcal{U}}_{qb}^\dagger$ . Analogously, we have

$$\begin{aligned} \hat{\Sigma}_z &\equiv \hat{\mathcal{R}}_{qb}^\dagger \hat{\sigma}_z \hat{\mathcal{R}}_{qb} \\ &= \hat{\sigma}_z \cos[2\eta(\hat{a} + \hat{a}^\dagger)] + \hat{\sigma}_y \sin[2\eta(\hat{a} + \hat{a}^\dagger)], \end{aligned} \quad (\text{A25})$$

$$\hat{\Sigma}_x \equiv \hat{\mathcal{R}}_{qb}^\dagger \hat{\sigma}_x \hat{\mathcal{R}}_{qb} = \hat{\sigma}_x. \quad (\text{A26})$$

A comparison between Eq. (A1) and Eq. (A23) clearly shows that  $\hat{S} = \omega_q \hat{\Sigma}_y$  and  $\hat{B}_k = \hat{c}_k + \hat{c}_k^\dagger$ .

By expanding the qubit operator  $\hat{\Sigma}_y$  in Eq. (A23) in the dressed representation, we obtain

$$\hat{H}_{qb} = \omega_q \sum_{m,l} (\Sigma_y)_{lm} \hat{P}'_{lm} \sum_k \eta_k^q (\hat{c}_k + \hat{c}_k^\dagger), \quad (\text{A27})$$

where  $(\Sigma_y)_{lm} = \langle l | \hat{\Sigma}_y | m \rangle$  are the matrix elements of the Pauli  $y$  operator, with  $|l\rangle$  being the energy eigenstates of the Rabi Hamiltonian in the Coulomb gauge [Eq. (1) in Sec. II A]. The matrix elements in Eq. (A27) satisfy the relation

$$\omega_q (\Sigma_y)_{lm} = i\omega_{ml} (\Sigma_x)_{lm}. \quad (\text{A28})$$

As done for the previous cavity-bath interaction Hamiltonian, we can expand the qubit dressed-operators in terms of positive and negative frequencies operators, such that, by applying the RWA, Eq. (A27) can be written as

$$\hat{H}_{qb} = i \sum_{m>l} \omega_{ml} (\Sigma_x)_{lm} \hat{P}'_{lm} \sum_k \eta_k^q \hat{c}_k^\dagger + \text{H.c.} \quad (\text{A29})$$

### b. Qubit-bath interaction in the dipole gauge

In the dipole gauge, the qubit-bath interaction Hamiltonian can be obtained by applying the generalized minimal-coupling replacement to the bosonic Hamiltonian for the bare field-bath  $\hat{H}_b = \sum_k \omega_k \hat{c}_k^\dagger \hat{c}_k$ . This corresponds to transforming the bath operators as follows:

$$c_k \rightarrow \hat{\mathcal{R}}_{qb} \hat{c}_k \hat{\mathcal{R}}_{qb}^\dagger = \hat{c}_k + i\eta_k^q \hat{\sigma}_x, \quad (\text{A30})$$

where  $\hat{\mathcal{R}}_{qb} = \hat{\mathcal{U}}_{qb}^\dagger$ . The resulting qubit-bath Hamiltonian in the dipole gauge becomes

$$\hat{H}'_{qb} = i\sigma_x \sum_k \omega_k \eta_k^q (\hat{c}_k^\dagger - \hat{c}_k). \quad (\text{A31})$$

A comparison between Eq. (A1) and Eq. (A31) clearly shows that  $\hat{S} = -i\hat{\Sigma}_x$  and  $\hat{B}_k = \omega_k (\hat{c}_k - \hat{c}_k^\dagger)$ .

By expanding  $\hat{\sigma}_x$  in the dressed representation, we obtain

$$\hat{H}'_{qb} = -i \sum_{m,l} (\sigma_x)'_{lm} \hat{P}'_{lm} \sum_k \omega_k \eta_k^q (\hat{c}_k - \hat{c}_k^\dagger), \quad (\text{A32})$$

where  $(\sigma_x)'_{lm} = \langle l' | \hat{\sigma}_x | m' \rangle$  are the matrix elements of the Pauli  $x$  operator, with  $|l'\rangle$  being the energy eigenstates of the Rabi Hamiltonian in dipole gauge [Eq. (10) in Sec. II B].

Finally, in terms of positive and negative frequencies of the qubit dressed-operators and applying the RWA, Eq. (A32) can be written as

$$\hat{H}'_{qb} = i \sum_{m'>l'} (\sigma_x)'_{lm} \hat{P}'_{lm} \sum_k \omega_k \eta_k^q \hat{c}_k^\dagger + \text{H.c.} \quad (\text{A33})$$

## APPENDIX B: GAUGE INVARIANCE OF THE GENERALIZED MASTER EQUATION

The GME [65] for strongly interacting hybrid quantum systems is developed using the basis of the system eigenstates (dressed states). Moreover, it does not make use of the secular approximation (post-trace rotating wave approximation). Thus, unlike the dressed master equation in Ref. [64], suitable for anharmonic systems, it is also valid for systems displaying harmonic or quasiharmonic spectra. This feature is essential to describe the system dynamics and the resulting spectra both at small and at very large (deep strong) values of the normalized coupling strength  $\eta$ . Here, we provide a demonstration of the

$$\begin{aligned} \mathcal{L}_g^{c(q)}\hat{\rho} = & \frac{1}{2} \sum_{\substack{j>k \\ l>m}} \left\{ \Gamma_{lm}^{c(q)} n_{ml}(\mathcal{T}_{c(q)}) [\hat{P}_{lm}\hat{\rho}\hat{P}_{kj} - \hat{P}_{kj}\hat{P}_{lm}\hat{\rho}] + \Gamma_{kj}^{c(q)} n_{jk}(\mathcal{T}_{c(q)}) [\hat{P}_{lm}\hat{\rho}\hat{P}_{kj} - \hat{\rho}\hat{P}_{kj}\hat{P}_{lm}] \right. \\ & \left. + \Gamma_{lm}^{c(q)} [n_{ml}(\mathcal{T}_{c(q)}) + 1] [\hat{P}_{kj}\hat{\rho}\hat{P}_{lm} - \hat{\rho}\hat{P}_{lm}\hat{P}_{kj}] + \Gamma_{kj}^{c(q)} [n_{jk}(\mathcal{T}_{c(q)}) + 1] [\hat{P}_{kj}\hat{\rho}\hat{P}_{lm} - \hat{P}_{lm}\hat{P}_{kj}\hat{\rho}] \right\}, \end{aligned} \quad (\text{B2})$$

with

$$n_{kj}(\mathcal{T}_{c(q)}) = \{\exp[\omega_{kj}/(\omega_{c(q)}\mathcal{T}_{c(q)})] - 1\}^{-1}, \quad (\text{B3})$$

which is the thermal populations of the cavity and qubit reservoirs calculated at the transition frequencies  $\omega_{kj}$ .

The cavity- and qubit-bath coupling rates determine both the losses and the incoherent pumping of the system. These rates depend on the specific interaction Hamiltonian (which describe the coupling between the system component and its bath) and on the density of the states of the relative bath.

For the cavity-bath rate, following the general derivation in Appendix A1a, and using Eq. (A10), we obtain

$$\Gamma_{kj}^c = 2\pi d_c(\omega_{kj}) |\omega_{kj}\eta^c(\omega_{kj})|^2 |\langle k|(\hat{a} + \hat{a}^\dagger)|j\rangle|^2, \quad (\text{B4})$$

where  $d_c(\omega_{kj})$  is the density of states of the bath calculated at the transition frequency  $\omega_{kj}$ . For any numerical calculations in the main text, we assume  $\eta_k^c \propto 1/\sqrt{\omega_k}$ , and  $d_c$  independent of  $\omega$ . Taking these assumptions into account and including all the constants in the rate  $\kappa$ , the cavity-bath coupling rate can be expressed as

$$\Gamma_{kj}^c = \kappa \frac{\omega_{kj}}{\omega_c} |\langle j|(\hat{a} + \hat{a}^\dagger)|k\rangle|^2. \quad (\text{B5})$$

It is clear that the cavity-bath interaction rates in Eq. (B4) and Eq. (B5) are gauge invariant. Analogously, from the general derivation in Appendix A2a, and using Eq. (A29) we obtain

$$\Gamma_{kj}^q = 2\pi d_q(\omega_{kj}) |\omega_{kj}\eta^q(\omega_{kj})|^2 |\langle k|\hat{\sigma}_x|j\rangle|^2. \quad (\text{B6})$$

Assuming  $\eta_k^q \propto 1/\sqrt{\omega_k}$ ,  $d_c$  independent of  $\omega$ , and including all the constants in the rate  $\gamma$ , the qubit-bath coupling rate can be expressed as

$$\Gamma_{kj}^q = \gamma \frac{\omega_{kj}}{\omega_q} |\langle j|\hat{\sigma}_x|k\rangle|^2. \quad (\text{B7})$$

### 1. Gauge invariance

In any coherent description of the light-matter interaction, the expectation value of any Hermitian operator  $\hat{O}$  that char-

GME gauge invariance. Within this approach, we guarantee the gauge invariance of matrix elements of the density matrix and expectation values, as well as the obtained emission rate and spectra.

We start by considering the GME in the Coulomb gauge for the Rabi model, which can be written as

$$\dot{\hat{\rho}} = -i[\hat{H}_R, \hat{\rho}] + \mathcal{L}_g \hat{\rho}, \quad (\text{B1})$$

where the dissipator  $\mathcal{L}_g$  contains two contributions,  $\mathcal{L}_g = \mathcal{L}_g^c + \mathcal{L}_g^q$ , arising from the cavity-bath (c) and the qubit-bath (q) interaction, respectively:

acterizes a property of the optical system has to be gauge invariant. Since the correct gauge transformation is described by a unitary operator  $\hat{U}$ , if  $|\psi\rangle$  is a quantum state in the Coulomb gauge, it is trivial to see that

$$\langle \psi | \hat{O} | \psi \rangle = \langle \psi' | \hat{O}' | \psi' \rangle, \quad (\text{B8})$$

where  $\hat{O}' = \hat{U}\hat{O}\hat{U}^\dagger$  and  $|\psi'\rangle = \hat{U}|\psi\rangle$  are a generic Hermitian operator and a ket state in the dipole gauge, respectively. In particular, by considering the definition of the density operator  $\hat{\rho} = \sum_m p_m |\psi_m\rangle\langle\psi_m|$  one can clearly see that, while the matrix elements  $p_m$  are gauge-invariant probabilities the quantum states  $|\psi_m\rangle$  are gauge dependent. If  $|\psi_m\rangle$  are obtained in the Coulomb gauge, in the dipole gauge we have

$$\hat{\rho}' = \sum_m p_m |\psi'_m\rangle\langle\psi'_m| = \hat{U}\hat{\rho}\hat{U}^\dagger. \quad (\text{B9})$$

Here, we show that the master equation in Eq. (B2) does not break gauge invariance. As done so far, we are labeling quantum states and operators in the dipole gauge with a prime apex primed superscript.

Due to the Eq. (B8), we want to show that the time evolution of any system operator is gauge invariant, namely,

$$\frac{d}{dt} \langle \hat{O} \rangle = \text{Tr} \hat{O} \dot{\hat{\rho}} = \text{Tr} \hat{O}' \dot{\hat{\rho}}'. \quad (\text{B10})$$

In terms of Eq. (B1), we can write Eq. (B10) in the Coulomb gauge as

$$\begin{aligned} \text{Tr} \hat{O} \dot{\hat{\rho}} &= -i \text{Tr} \hat{O} [\hat{H}_R, \hat{\rho}] + \text{Tr} \hat{O} \mathcal{L}_g \hat{\rho} \\ &= -i \sum_j \langle j | \hat{O} [\hat{H}_R, \hat{\rho}] | j \rangle + \sum_j \langle j | \hat{O} \mathcal{L}_g \hat{\rho} | j \rangle. \end{aligned} \quad (\text{B11})$$

Let us next consider separately the two terms on the right-hand side of Eq. (B11). By means of the unitary gauge

transformation  $\hat{U}$ , we obtain

$$\begin{aligned} \sum_j \langle j | \hat{O}(\hat{H}_R \hat{\rho} - \hat{\rho} \hat{H}_R) | j \rangle &= \sum_j \langle j' | [\hat{U} \hat{U}^\dagger (\hat{U} \hat{O} \hat{U}^\dagger) (\hat{U} \hat{H}_R \hat{U}^\dagger) (\hat{U} \hat{\rho} \hat{U}^\dagger) - (\hat{U} \hat{\rho} \hat{U}^\dagger) (\hat{U} \hat{H}_R \hat{U}^\dagger) \hat{U} \hat{U}^\dagger] | j' \rangle \\ &= \sum_j \langle j' | \hat{O}'(\hat{H}'_R \hat{\rho}' - \hat{\rho}' \hat{H}'_R) | j' \rangle = \text{Tr} \hat{O}'[\hat{H}'_R, \hat{\rho}']'. \end{aligned} \quad (\text{B12})$$

To deal with the second term on the right-hand side of Eq. (B11), we first observe that  $\Gamma_{ml}^{c(q)} = \Gamma_{m'l'}^{c(q)}$  and  $n_{ml}(\mathcal{T}_{c(q)}) = n_{m'l'}(\mathcal{T}_{c(q)})$  in Eq. (B2) are gauge invariant. Thus, it is sufficient to show that the terms in the square brackets (involving the transition operators  $\hat{P}_{lm}$ ) in Eq. (B2), provide gauge-invariant contributions in Eq. (B10). Considering the first of these terms, we have

$$\begin{aligned} \text{Tr} \hat{O} \hat{P}_{lm} \hat{\rho} \hat{P}_{kj} &= \sum_n \langle j | \hat{O} \hat{P}_{lm} \hat{\rho} \hat{P}_{kj} | j \rangle = \sum_n \langle j' | \hat{U} \hat{U}^\dagger (\hat{U} \hat{O} \hat{U}^\dagger) (\hat{U} \hat{P}_{lm} \hat{U}^\dagger) (\hat{U} \hat{\rho} \hat{U}^\dagger) (\hat{U} \hat{P}_{kj} \hat{U}^\dagger) \hat{U} \hat{U}^\dagger | j' \rangle \\ &= \sum_n \langle j' | \hat{O}' \hat{P}'_{lm} \hat{\rho}' \hat{P}'_{kj} | j' \rangle = \text{Tr} \hat{O}' \hat{P}'_{lm} \hat{\rho}' \hat{P}'_{kj}'. \end{aligned} \quad (\text{B13})$$

It is easy to see that the other similar terms transform exactly in the same way. This proves that

$$\text{Tr} \hat{O} \mathcal{L}_g \hat{\rho} = \text{Tr} \hat{O}' \mathcal{L}'_g \hat{\rho}',$$

and, as a consequence, Eq. (B10) is gauge invariant.

### APPENDIX C: CAVITY AND QUBIT EMISSION RATES AND SPECTRA AT POSITIVE DETUNING ( $\Delta = 0.3$ )

We now present numerically calculated emission rates and spectra obtained in the case of significant qubit-cavity detuning  $\Delta$ , in normalized units. In particular, here we consider the cases of  $\Delta = 0.3$ .

The emission rates versus the normalized coupling strength  $\eta$ , for the positive-detuning case and for both the cavity and the qubit, are shown in Fig. 13 at both low and higher effective temperatures. For both the considered temperatures, the cavity emission rate never exceeds the qubit one. At  $\mathcal{T}_q = 5 \times 10^{-2}$ , the peak qubit emission rate exceeds the cavity peak by more than two orders of magnitude. The increase of the cavity emission rate at increasing values of  $\eta$  (Purcell effect) continues until the onset of the USC regime, and the plateau in the strong-coupling regime, observed at zero detuning, is here absent. At  $\mathcal{T}_q = 5 \times 10^{-2}$ , the qubit emission rate reaches in the USC regime values, which are about six orders of magnitude larger than  $W_q^0$ .

Looking at Fig. 14, we observe that, at weak-coupling strengths the  $(\tilde{1}_-, 0)$  transition almost coincides with the qubit transition frequency, while the  $(\tilde{1}_+, 0)$  almost coincides with the resonance frequency of the cavity mode. Figure 15 shows the cavity emission spectrum, obtained at the effective temperature  $\mathcal{T}_q = 5 \times 10^{-2}$ , in the weak- and strong-coupling regimes. In the frequency region displayed in Fig. 15, the only visible emission line corresponds to the transition  $(\tilde{1}_-, 0)$ . As in the negative-detuning case (see Fig. 9), in the weak-coupling regime, the emission originates from the qubit-like transition  $(\tilde{1}_-, 0)$ , which, however, now is the lowest-energy transition.

Figure 16 shows the logarithmic cavity emission spectra  $S_c(\omega)$  as a function of the normalized coupling strength  $\eta$ , ranging from the strong to the DSC regimes. At very low effective temperatures, the emission originates almost only

from the lowest energy transition  $(\tilde{1}_-, 0)$ , because the photon-like transition  $(\tilde{1}_+, 0)$  is at higher energy and, owing to the detuning, is poorly hybridized with the qubit excited state, at least for moderate coupling strengths. Increasing the effective temperature ( $\mathcal{T}_q = 0.2$ ) higher energy levels start to get populated, thus determining the appearance of several additional emission lines [see Fig. 14(b)]. The qubit emission spectra versus  $\eta$ , at  $\mathcal{T}_q = 0.2$  are shown in Fig. 17. The line

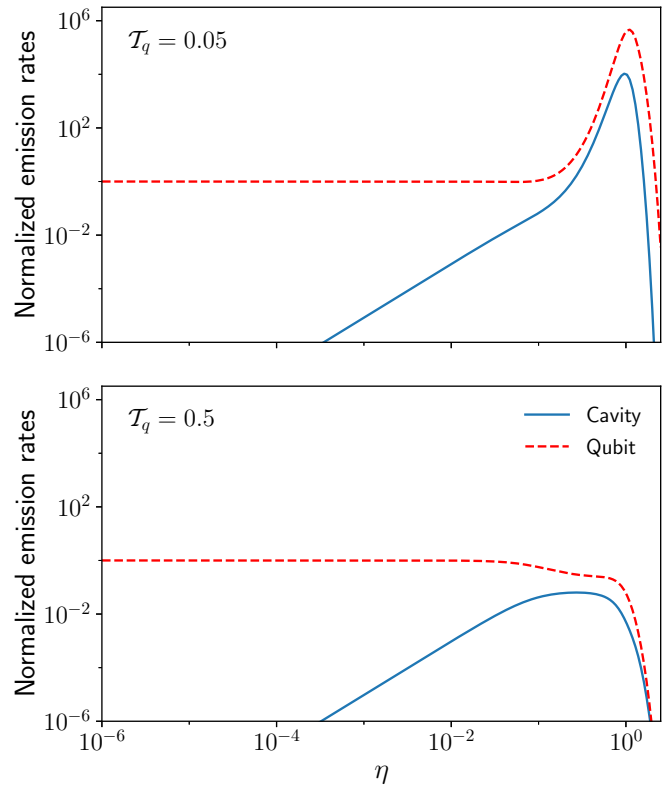


FIG. 13. Cavity and qubit emission rates (normalized with respect to the qubit emission rate  $W_q^0$  calculated for  $\eta = 0$ )  $\mathcal{W}_c = W_c/W_q^0$  (blue continuous curve), and  $\mathcal{W}_q = W_q/W_q^0$  (red dashed) versus the light-matter normalized coupling strength  $\eta$ . We used  $\Delta = 0.3$ , corresponding to  $\omega_c/\omega_q = 1.3$ . The upper panel is for  $\mathcal{T}_q = 5 \times 10^{-2}$ , the lower panel is for  $\mathcal{T}_q = 5 \times 10^{-1}$ .

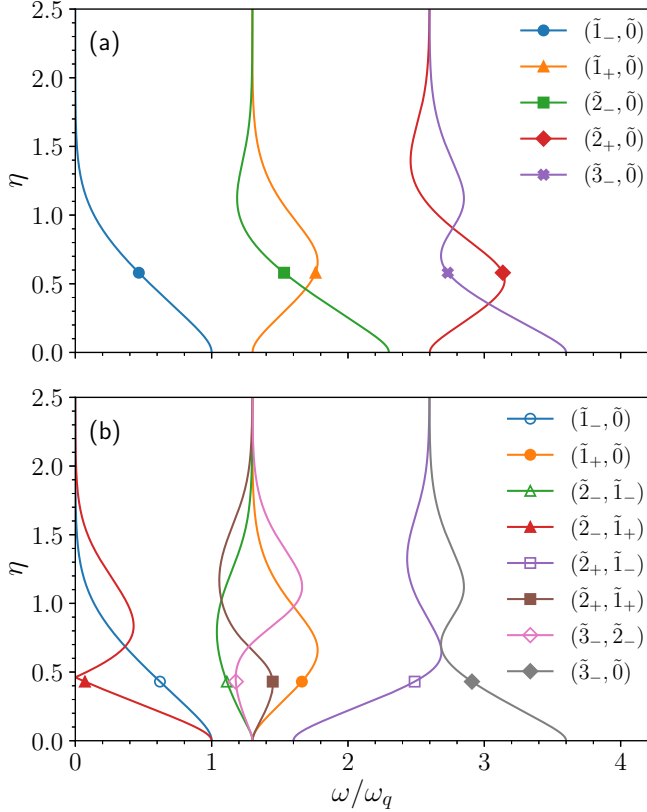


FIG. 14. Normalized energy levels and transition energies versus  $\eta$  for  $\Delta = 0.3$  ( $\omega_c/\omega_q = 1.3$ ). (a) Lowest normalized energy levels (with the ground-state energy as reference)  $\omega_{j\pm} - \bar{\omega}_0$  of the QRM. (b) Normalized parity-allowed transition energies  $|\omega_{j\pm} - \omega_{k\pm}|$  for the lowest eigenstates of the QRM.

corresponding to the transition  $(\tilde{1}_+, 0)$  is the brightest at any coupling strength where emission lines are visible. Also in this case, the flat background qubit emission in the DSC regime dominates.

#### APPENDIX D: COMPARISON WITH OTHER MODELS

In this section, we present examples of calculations of cavity and qubit emission spectra, (using the same parameters adopted in the previous section) obtained using different models and/or dissipators for the master equation. In particular, we present (i) some spectra obtained by using the JCM and the standard master equation for cavity QED, with the dissipators obtained by neglecting the light-matter interaction [64]. (ii) We also present spectra obtained with the same model used in Sec. III by using a master equation where the dissipators have been obtained taking into account the light-matter interaction, but applying the post-trace RWA [64].

##### 1. Jaynes-Cummings model

The JCM is the simplest model describing a two-level system interacting with a quantized single-mode of an electromagnetic resonator. It is obtained applying the RWA to the QRM in the dipole gauge. Therefore, it is expected to be valid only for coupling strengths below the USC regime. The JC

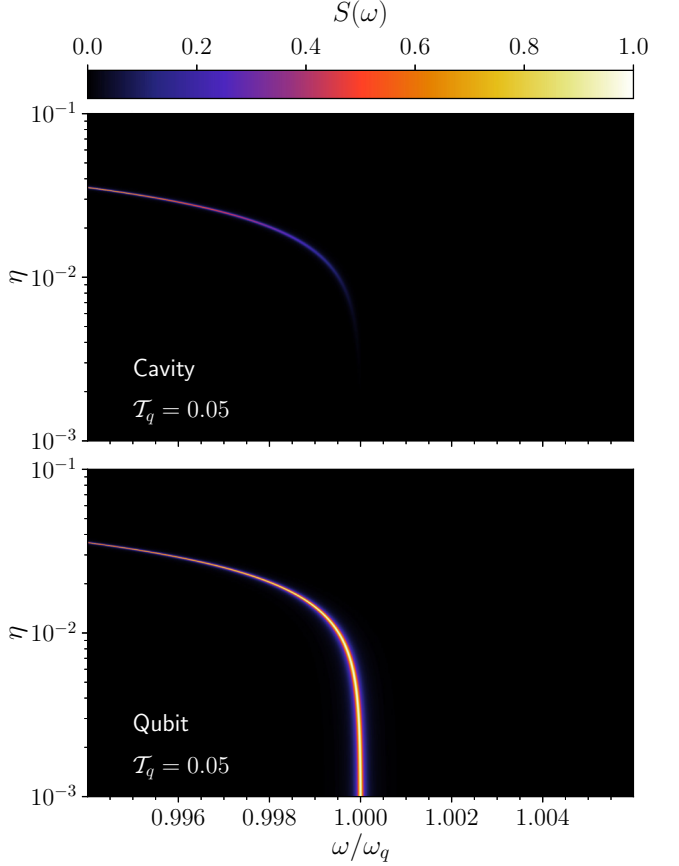


FIG. 15. Cavity  $S_c(\omega)$  and qubit  $S_q(\omega)$  emission spectra in the weak- and strong-coupling regime, calculated for  $10^{-3} < \eta < 10^{-1}$  and for  $\Delta = 0.3$  ( $\omega_c/\omega_q = 1.3$ ). The spectra have been obtained under weak incoherent excitation of the qubit. We used an effective qubit temperature  $\mathcal{T}_q = 5 \times 10^{-2}$ . The spectra have been normalized so that the highest peak in each density plot is set at 1.

Hamiltonian is

$$\hat{\mathcal{H}}_{JC} = \omega_c \hat{a}^\dagger \hat{a} + \frac{\omega_q}{2} \hat{\sigma}_z + \frac{\eta \omega_c}{2} (\hat{a} \hat{\sigma}_+ + \hat{a}^\dagger \hat{\sigma}_-). \quad (D1)$$

In addition, to describe the interaction of the qubit-cavity system with the environment, we used the standard quantum optical master equation

$$\dot{\hat{\rho}} = -i[\hat{\mathcal{H}}_{JC}, \hat{\rho}] + \mathcal{L}_{\text{bare}}^c \hat{\rho} + \mathcal{L}_{\text{bare}}^q \hat{\rho}, \quad (D2)$$

where  $\mathcal{L}_{\text{bare}}^c$  and  $\mathcal{L}_{\text{bare}}^q$  are the standard dissipators for the cavity and the qubit respectively:

$$\begin{aligned} \mathcal{L}_{\text{bare}}^c \hat{\rho} &= \kappa [1 + n_c(\mathcal{T}_c)] \mathcal{D}[\hat{a}] \hat{\rho} \\ &\quad + \kappa n_c(\mathcal{T}_c) \mathcal{D}[\hat{a}^\dagger] \hat{\rho}, \\ \mathcal{L}_{\text{bare}}^q \hat{\rho} &= \gamma [1 + n_q(\mathcal{T}_q)] \mathcal{D}[\hat{\sigma}_-] \hat{\rho} \\ &\quad + \gamma n_q(\mathcal{T}_q) \mathcal{D}[\hat{\sigma}_+] \hat{\rho}. \end{aligned} \quad (D3)$$

The term  $n_{c(q)}(\mathcal{T}_{c(q)}) = [\exp(1/\mathcal{T}_{c(q)}) - 1]^{-1}$  is the thermal population, and  $\mathcal{D}[\hat{O}]$  indicates the generic dissipator

$$\mathcal{D}[\hat{O}] \hat{\rho} = \frac{1}{2} (2\hat{O}\hat{\rho}\hat{O}^\dagger - \hat{\rho}\hat{O}^\dagger\hat{O} - \hat{O}^\dagger\hat{O}\hat{\rho}). \quad (D4)$$

In this case, the cavity and qubit emission rates are simply proportional to  $W_c(t) = \langle \hat{a}^\dagger \hat{a} \rangle_t$  and  $W_q(t) = \langle \hat{\sigma}_+ \hat{\sigma}_- \rangle_t$ , respec-

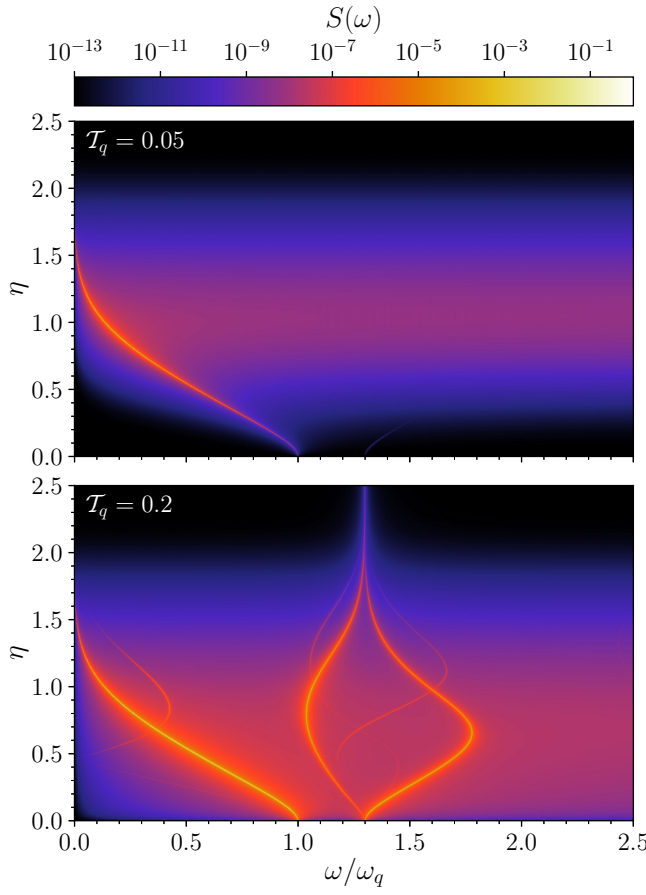


FIG. 16. Cavity emission spectra  $S_c(\omega)$  for values of  $\eta$  reaching the USC and DSC regimes obtained for two different effective qubit temperatures  $T_q = 0.05, 0.2$ . We used  $\Delta = 0.3$  ( $\omega_c/\omega_q = 1.3$ ). The spectra have been normalized so that the highest peak in each density plot is set at 1. Increasing the temperature, additional lines originating from transitions involving higher energy levels appear. Most of them correspond to transition energies shown in Fig. 10.

tively. Analogously, the steady-state cavity and qubit emission spectra can be defined as

$$\begin{aligned} \tilde{S}_c(\omega) &= \text{Re} \int_0^\infty d\tau e^{-i\omega\tau} \langle \hat{a}^\dagger(t+\tau)\hat{a}(t) \rangle_{ss}, \\ \tilde{S}_q(\omega) &= \text{Re} \int_0^\infty d\tau e^{-i\omega\tau} \langle \hat{\sigma}_+(t+\tau)\hat{\sigma}_-(t) \rangle_{ss}. \end{aligned} \quad (\text{D5})$$

Figure 18 describes the normalized emission spectra of the cavity in the weak- and strong-coupling range. As mentioned above, the JCM is a good approximation in this range of coupling strengths. The only difference with respect to the results obtained using the full QRM (see Fig. 4) is the lack of any intensity difference between the split lines originating from the transitions  $(1_-, 0)$  and  $(1_+, 0)$ . Actually, the reason is not directly due to the use of the JCM, but is a consequence of using the standard master equation which does not include bath populations calculated at the system transition frequencies. Of course such a model cannot provide reliable results beyond the strong-coupling regime (see Fig. 19).

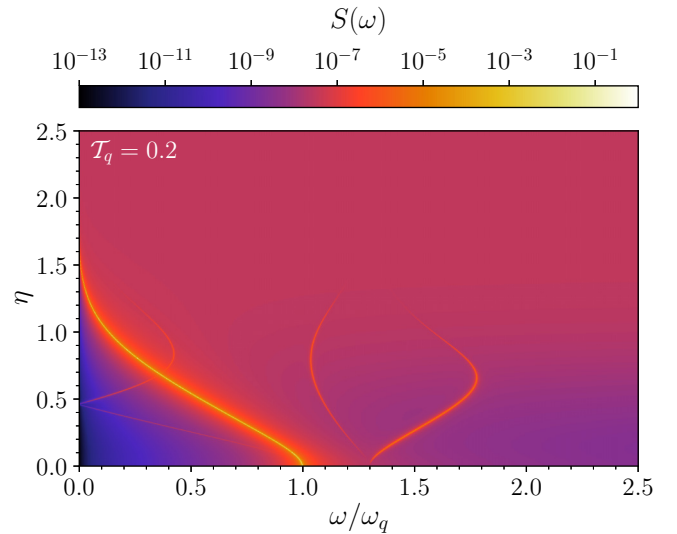


FIG. 17. Qubit emission spectra  $S_q(\omega)$  for values of  $\eta$  reaching the USC and DSC regimes obtained at  $T_q = 0.2$ . We used  $\Delta = 0.3$  ( $\omega_c/\omega_q = 1.3$ ). The spectra have been normalized so that the highest peak is set at 1. The visible lines correspond to transition energies shown in Fig. 2. The origin of the flat (red) signal background for  $\eta > 1.5$  is explained in the text [see Eq. (28)].

## 2. Dressed master equation with post-trace rotating-wave approximation

The standard quantum-optics master equation has several weaknesses, and one of the most relevant is that the interaction between the subsystems is not considered when deriving the dissipators [86]. One of the main drawbacks is that, owing to the presence of counter-rotating terms in the Hamiltonian describing the interaction between the light and matter components of the system, unphysical excitations are generated

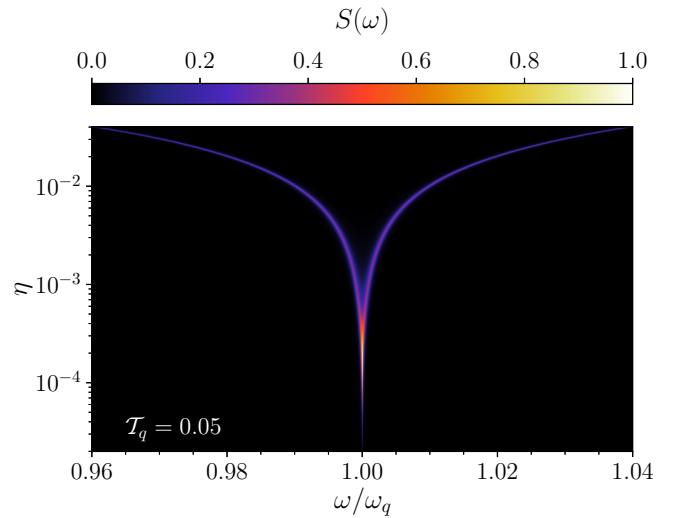


FIG. 18. Cavity emission spectra  $S_c(\omega)$  in the weak- and strong-coupling regime for the JCM, calculated for  $2 \times 10^{-5} < \eta < 4 \times 10^{-2}$  and for  $\Delta = 0$ . The spectra have been obtained under weak incoherent excitation of the qubit. We used an effective qubit temperature  $T_q = 5 \times 10^{-2}$ . The spectra have been normalized, so that the highest peak in each density plot is set at 1.

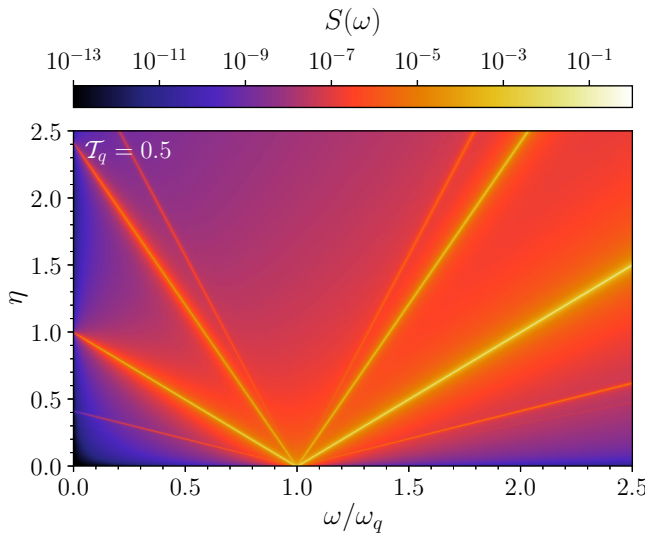


FIG. 19. Cavity emission spectra  $S_c(\omega)$  for values of  $\eta$  reaching the USC and DSC regimes with the JCM, obtained with an effective qubit temperature  $\mathcal{T}_q = 0.5$ . We used  $\Delta = 0$ . The spectra have been normalized, so that the highest peak in each density plot is set at 1. As predicted, the model drastically fails above the USC regime.

in the system even by a zero-temperature reservoir. For this reason, a dressed master equation was developed [64]. This model takes into account that transitions in the hybrid system occur between dressed eigenstates, and not between the eigenstates of the free Hamiltonians of the components.

The dressed-state master equation is

$$\dot{\hat{\rho}} = -i[\hat{\mathcal{H}}_R, \hat{\rho}] + \mathcal{L}_{\text{dressed}}\hat{\rho}, \quad (\text{D6})$$

where  $\mathcal{L}_{\text{dressed}}$  is of the form

$$\begin{aligned} \mathcal{L}_{\text{dressed}}\hat{\rho} = & \sum_{i=c,q} \sum_{k>j} \left\{ \Gamma_{kj}^i [1 + n_{kj}(\mathcal{T}_i)] \mathcal{D}[|j\rangle\langle k|] \hat{\rho} \right. \\ & \left. + \Gamma_{kj}^i n_{kj}(\mathcal{T}_i) \mathcal{D}[|k\rangle\langle j|] \hat{\rho} \right\}. \end{aligned} \quad (\text{D7})$$

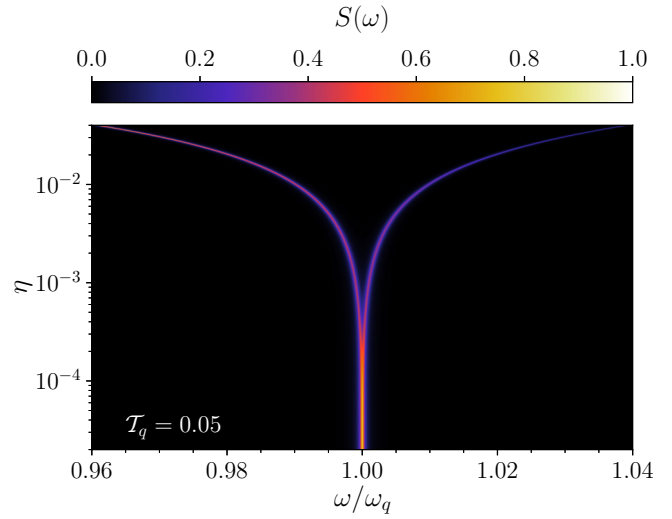


FIG. 20. Cavity emission spectra  $S_c(\omega)$  in the weak- and strong-coupling regime using the dressed master equation, calculated for  $2 \times 10^{-5} < \eta < 4 \times 10^{-2}$  and for  $\Delta = 0$ . The spectra have been obtained under weak incoherent excitation of the qubit. We used an effective qubit temperature  $\mathcal{T}_q = 5 \times 10^{-2}$ . The spectra have been normalized, so that the highest peak in each density plot is set at 1.

The terms  $n_{kj}(\mathcal{T}_i)$  are the thermal reservoir populations [see Eq. (B3)], calculated at the system transition frequencies  $\omega_{kj}$ , and  $\Gamma_{kj}^{c(q)}$  are the cavity and qubit decay [see Eq. (B5) and Eq. (B7)].

As mentioned above, this dissipation model is valid only with anharmonic systems and, as can be noticed in Fig. 20, it returns incorrect results when the coupling is very weak and the system displays a quasiharmonic spectrum—that is, a nonzero cavity photon emission at negligible couplings [compare with Fig. 4(a)].

Beyond the strong-coupling regime, this model shows no significant differences, since the energy spectrum of the system becomes anharmonic in this coupling regime.

- 
- [1] E. Jaynes and F. Cummings, Comparison of quantum and semi-classical radiation theories with application to the beam maser, *Proc. IEEE* **51**, 89 (1963).
- [2] I. I. Rabi, On the process of space quantization, *Phys. Rev.* **49**, 324 (1936).
- [3] A. F. Kockum, A. Miranowicz, S. De Liberato, S. Savasta, and F. Nori, Ultrastrong coupling between light and matter, *Nat. Rev. Phys.* **1**, 19 (2019).
- [4] P. Forn-Díaz, L. Lamata, E. Rico, J. Kono, and E. Solano, Ultrastrong coupling regimes of light-matter interaction, *Rev. Mod. Phys.* **91**, 025005 (2019).
- [5] S. Hughes, Breakdown of the Area Theorem: Carrier-Wave Rabi Flopping of Femtosecond Optical Pulses, *Phys. Rev. Lett.* **81**, 3363 (1998).
- [6] S. Haroche and J. M. Raimond, *Exploring the Quantum: Atoms, Cavities and Photons* (Oxford University Press, 2006).
- [7] E. M. Purcell, H. C. Torrey, and R. V. Pound, Resonance absorption by nuclear magnetic moments in a solid, *Phys. Rev.* **69**, 37 (1946).
- [8] K. J. Vahala, Optical microcavities, *Nature (London)* **424**, 839 (2003).
- [9] C. Salter, R. Stevenson, I. Farrer, C. Nicoll, D. Ritchie, and A. Shields, An entangled-light-emitting diode, *Nature (London)* **465**, 594 (2010).
- [10] N. Somaschi *et al.*, Near-optimal single-photon sources in the solid state, *Nat. Photonics* **10**, 340 (2016).
- [11] S. Haroche, Nobel lecture: Controlling photons in a box and exploring the quantum to classical boundary, *Rev. Mod. Phys.* **85**, 1083 (2013).
- [12] I. Buluta, S. Ashhab, and F. Nori, Natural and artificial atoms for quantum computation, *Rep. Prog. Phys.* **74**, 104401 (2011).

- [13] I. Georgescu and F. Nori, Quantum technologies: An old new story, *Phys. World* **25**, 16 (2012).
- [14] G. Günter, A. Anappara, J. Hees, A. Sell, G. Biasiol, L. Sorba, S. De Liberato, C. Ciuti, A. Tredicucci, A. Leitenstorfer, and R. Huber, Sub-cycle switch-on of ultrastrong light-matter interaction, *Nature (London)* **458**, 178 (2009).
- [15] P. Forn-Díaz, J. Lisenfeld, D. Marcos, J. J. García-Ripoll, E. Solano, C. J. P. M. Harmans, and J. E. Mooij, Observation of the Bloch-Siegert Shift in a Qubit-Oscillator System in the Ultrastrong Coupling Regime, *Phys. Rev. Lett.* **105**, 237001 (2010).
- [16] Y. Todorov, A. M. Andrews, R. Colombelli, S. De Liberato, C. Ciuti, P. Klang, G. Strasser, and C. Sirtori, Ultrastrong Light-Matter Coupling Regime with Polariton Dots, *Phys. Rev. Lett.* **105**, 196402 (2010).
- [17] T. Schwartz, J. A. Hutchison, C. Genet, and T. W. Ebbesen, Reversible Switching of Ultrastrong Light-Molecule Coupling, *Phys. Rev. Lett.* **106**, 196405 (2011).
- [18] J. You and F. Nori, Atomic physics and quantum optics using superconducting circuits, *Nature (London)* **474**, 589 (2011).
- [19] G. Scalari, C. Maissen, D. Turčinková, D. Hagemüller, S. De Liberato, C. Ciuti, C. Reichl, D. Schuh, W. Wegscheider, M. Beck, and J. Faist, Ultrastrong coupling of the cyclotron transition of a 2D electron gas to a THz metamaterial, *Science* **335**, 1323 (2012).
- [20] M. Geiser, F. Castellano, G. Scalari, M. Beck, L. Nevou, and J. Faist, Ultrastrong Coupling Regime and Plasmon Polaritons in Parabolic Semiconductor Quantum Wells, *Phys. Rev. Lett.* **108**, 106402 (2012).
- [21] S. Kéna-Cohen, S. A. Maier, and D. D. C. Bradley, Ultrastrongly coupled exciton-polaritons in metal-clad organic semiconductor microcavities, *Adv. Opt. Mater.* **1**, 827 (2013).
- [22] Z.-L. Xiang, S. Ashhab, J. Q. You, and F. Nori, Hybrid quantum circuits: Superconducting circuits interacting with other quantum systems, *Rev. Mod. Phys.* **85**, 623 (2013).
- [23] C. Maissen, G. Scalari, F. Valmorra, M. Beck, J. Faist, S. Cibella, R. Leoni, C. Reichl, C. Charpentier, and W. Wegscheider, Ultrastrong coupling in the near field of complementary split-ring resonators, *Phys. Rev. B* **90**, 205309 (2014).
- [24] M. Goryachev, W. G. Farr, D. L. Creedon, Y. Fan, M. Kostylev, and M. E. Tobar, High-Cooperativity Cavity QED with Magnons at Microwave Frequencies, *Phys. Rev. Appl.* **2**, 054002 (2014).
- [25] J. Pirkkalainen, S. Cho, F. Massel, J. Tuorila, T. Heikkilä, P. Hakonen, and M. Sillanpää, Cavity optomechanics mediated by a quantum two-level system, *Nat. Commun.* **6**, 6981 (2015).
- [26] A. Baust, E. Hoffmann, M. Haeberlein, M. J. Schwarz, P. Eder, J. Goetz, F. Wulschner, E. Xie, L. Zhong, F. Quijandría, D. Zueco, J.-J. García Ripoll, L. García-Álvarez, G. Romero, E. Solano, K. G. Fedorov, E. P. Menzel, F. Deppe, A. Marx, and R. Gross, Ultrastrong coupling in two-resonator circuit QED, *Phys. Rev. B* **93**, 214501 (2016).
- [27] F. Benz *et al.*, Single-molecule optomechanics in picocavities, *Science* **354**, 726 (2016).
- [28] J. George, T. Chervy, A. Shalabney, E. Devaux, H. Hiura, C. Genet, and T. W. Ebbesen, Multiple Rabi Splittings under Ultrastrong Vibrational Coupling, *Phys. Rev. Lett.* **117**, 153601 (2016).
- [29] P. Forn-Díaz, J. García-Ripoll, B. Peropadre, J.-L. Orgiazzi, M. Yurtalan, R. Belyansky, C. Wilson, and A. Lupascu, Ultrastrong coupling of a single artificial atom to an electromagnetic continuum in the nonperturbative regime, *Nat. Phys.* **13**, 39 (2017).
- [30] F. Yoshihara, T. Fuse, S. Ashhab, K. Kakuyanagi, S. Saito, and K. Semba, Superconducting qubit-oscillator circuit beyond the ultrastrong-coupling regime, *Nat. Phys.* **13**, 44 (2017).
- [31] F. Yoshihara, T. Fuse, S. Ashhab, K. Kakuyanagi, S. Saito, and K. Semba, Characteristic spectra of circuit quantum electrodynamics systems from the ultrastrong- to the deep-strong-coupling regime, *Phys. Rev. A* **95**, 053824 (2017).
- [32] A. Bayer, M. Pozimski, S. Schambeck, D. Schuh, R. Huber, D. Bougeard, and C. Lange, Terahertz light-matter interaction beyond unity coupling strength, *Nano Lett.* **17**, 6340 (2017).
- [33] B. Askenazi, A. Vasanelli, Y. Todorov, E. Sakat, J.-J. Greffet, G. Beaudoin, I. Sagnes, and C. Sirtori, Midinfrared ultrastrong light-matter coupling for THz thermal emission, *ACS Photonics* **4**, 2550 (2017).
- [34] F. Barachati, J. Simon, Y. A. Getmanenko, S. Barlow, S. R. Marder, and S. Kéna-Cohen, Tunable third-harmonic generation from polaritons in the ultrastrong coupling regime, *ACS Photonics* **5**, 119 (2018).
- [35] F. Yoshihara, T. Fuse, Z. Ao, S. Ashhab, K. Kakuyanagi, S. Saito, T. Aoki, K. Koshino, and K. Semba, Inversion of Qubit Energy Levels in Qubit-Oscillator Circuits in the Deep-Strong-Coupling Regime, *Phys. Rev. Lett.* **120**, 183601 (2018).
- [36] E. Eizner, J. Brodeur, F. Barachati, A. Sridharan, and S. Kéna-Cohen, Organic photodiodes with an extended responsivity using ultrastrong light-matter coupling, *ACS Photonics* **5**, 2921 (2018).
- [37] G. L. Paravicini-Bagliani, F. Appugliese, E. Richter, F. Valmorra, J. Keller, M. Beck, N. Bartolo, C. Rössler, T. Ihn, K. Ensslin, C. Ciuti, G. Scalari, and J. Faist, Magneto-transport controlled by Landau polariton states, *Nat. Phys.* **15**, 186 (2019).
- [38] J. Puertas Martínez, S. Léger, N. Geeraert, R. Dassonneville, L. Planat, F. Foroughi, Y. Krupko, O. Buisson, C. Naud, W. Hasch-Guichard, S. Florens, I. Snyman, and N. Roch, A tunable Josephson platform to explore many-body quantum optics in circuit-QED, *npj Quantum Inf.* **5**, 19 (2019).
- [39] G. Flower, M. Goryachev, J. Bourhill, and M. E. Tobar, Experimental implementations of cavity-magnon systems: From ultra strong coupling to applications in precision measurement, *New J. Phys.* **21**, 095004 (2019).
- [40] M. Jeannin, G. Mariotti Nesurini, S. Suffit, D. Gacemi, A. Vasanelli, L. Li, A. G. Davies, E. Linfield, C. Sirtori, and Y. Todorov, Ultrastrong light-matter coupling in deeply subwavelength THz LC resonators, *ACS Photonics* **6**, 1207 (2019).
- [41] S.-P. Wang, G.-Q. Zhang, Y. Wang, Z. Chen, T. Li, J. S. Tsai, S.-Y. Zhu, and J. Q. You, Photon-Dressed Bloch-Siegert Shift in an Ultrastrongly Coupled Circuit Quantum Electrodynamical System, *Phys. Rev. Appl.* **13**, 054063 (2020).
- [42] J. Keller, G. Scalari, F. Appugliese, S. Rajabali, M. Beck, J. Haase, C. A. Lehner, W. Wegscheider, M. Failla, M. Myronov, D. R. Leadley, J. Lloyd-Hughes, P. Nataf, and J. Faist, Landau polaritons in highly nonparabolic two-dimensional gases in the ultrastrong coupling regime, *Phys. Rev. B* **101**, 075301 (2020).
- [43] K. K. W. Ma and C. K. Law, Three-photon resonance and adiabatic passage in the large-detuning Rabi model, *Phys. Rev. A* **92**, 023842 (2015).

- [44] A. F. Kockum, A. Miranowicz, V. Macrì, S. Savasta, and F. Nori, Deterministic quantum nonlinear optics with single atoms and virtual photons, *Phys. Rev. A* **95**, 063849 (2017).
- [45] A. F. Kockum, V. Macrì, L. Garziano, S. Savasta, and F. Nori, Frequency conversion in ultrastrong cavity QED, *Sci. Rep.* **7**, 5313 (2017).
- [46] R. Stassi, V. Macrì, A. F. Kockum, O. Di Stefano, A. Miranowicz, S. Savasta, and F. Nori, Quantum nonlinear optics without photons, *Phys. Rev. A* **96**, 023818 (2017).
- [47] V. Macrì, A. Ridolfo, O. Di Stefano, A. F. Kockum, F. Nori, and S. Savasta, Nonperturbative Dynamical Casimir Effect in Optomechanical Systems: Vacuum Casimir-Rabi Splittings, *Phys. Rev. X* **8**, 011031 (2018).
- [48] O. Di Stefano, A. Settineri, V. Macrì, A. Ridolfo, R. Stassi, A. F. Kockum, S. Savasta, and F. Nori, Interaction of Mechanical Oscillators Mediated by the Exchange of Virtual Photon Pairs, *Phys. Rev. Lett.* **122**, 030402 (2019).
- [49] L. Garziano, R. Stassi, V. Macrì, A. F. Kockum, S. Savasta, and F. Nori, Multiphoton quantum Rabi oscillations in ultrastrong cavity QED, *Phys. Rev. A* **92**, 063830 (2015).
- [50] L. Garziano, V. Macrì, R. Stassi, O. Di Stefano, F. Nori, and S. Savasta, One Photon Can Simultaneously Excite Two or More Atoms, *Phys. Rev. Lett.* **117**, 043601 (2016).
- [51] V. Macrì, F. Nori, S. Savasta, and D. Zueco, Spin squeezing by one-photon–two-atom excitation processes in atomic ensembles, *Phys. Rev. A* **101**, 053818 (2020).
- [52] S. De Liberato, Light-Matter Decoupling in the Deep Strong Coupling Regime: the Breakdown of the Purcell Effect, *Phys. Rev. Lett.* **112**, 016401 (2014).
- [53] Y. Ashida, A. İmamoğlu, and E. Demler, Cavity Quantum Electrodynamics at Arbitrary Light-Matter Coupling Strengths, *Phys. Rev. Lett.* **126**, 153603 (2021).
- [54] N. S. Mueller, Y. Okamura, B. G. M. Vieira, S. Juergensen, H. Lange, E. B. Barros, F. Schulz, and S. Reich, Deep strong light-matter coupling in plasmonic nanoparticle crystals, *Nature (London)* **583**, 780 (2020).
- [55] J. J. García-Ripoll, B. Peropadre, and S. De Liberato, Light-matter decoupling and  $A^2$  term detection in superconducting circuits, *Sci. Rep.* **5**, 16055 (2015).
- [56] A. Vukics, T. Grießer, and P. Domokos, Elimination of the A-Square Problem from Cavity QED, *Phys. Rev. Lett.* **112**, 073601 (2014).
- [57] D. De Bernardis, P. Pilar, T. Jaako, S. De Liberato, and P. Rabl, Breakdown of gauge invariance in ultrastrong-coupling cavity QED, *Phys. Rev. A* **98**, 053819 (2018).
- [58] A. Stokes and A. Nazir, Gauge ambiguities imply Jaynes-Cummings physics remains valid in ultrastrong coupling QED, *Nat. Commun.* **10**, 499 (2019).
- [59] O. Di Stefano, A. Settineri, V. Macrì, L. Garziano, R. Stassi, S. Savasta, and F. Nori, Resolution of gauge ambiguities in ultrastrong-coupling cavity quantum electrodynamics, *Nat. Phys.* **15**, 803 (2019).
- [60] L. Garziano, A. Settineri, O. Di Stefano, S. Savasta, and F. Nori, Gauge invariance of the Dicke and Hopfield models, *Phys. Rev. A* **102**, 023718 (2020).
- [61] S. Savasta, O. Di Stefano, A. Settineri, D. Zueco, S. Hughes, and F. Nori, Gauge principle and gauge invariance in two-level systems, *Phys. Rev. A* **103**, 053703 (2021).
- [62] A. Settineri, O. Di Stefano, D. Zueco, S. Hughes, S. Savasta, and F. Nori, Gauge freedom, quantum measurements, and time-dependent interactions in cavity QED, *Phys. Rev. Research* **3**, 023079 (2021).
- [63] W. Salmon, C. Gustin, A. Settineri, O. Di Stefano, D. Zueco, S. Savasta, F. Nori, and S. Hughes, Gauge-independent emission spectra and quantum correlations in the ultrastrong coupling regime of cavity-QED, *arXiv:2102.12055*.
- [64] F. Beaudoin, J. Gambetta, and A. Blais, Dissipation and ultrastrong coupling in circuit QED, *Phys. Rev. A* **84**, 043832 (2011).
- [65] A. Settineri, V. Macrì, A. Ridolfo, O. Di Stefano, A. F. Kockum, F. Nori, and S. Savasta, Dissipation and thermal noise in hybrid quantum systems in the ultrastrong-coupling regime, *Phys. Rev. A* **98**, 053834 (2018).
- [66] O. Di Stefano, R. Stassi, L. Garziano, A. F. Kockum, S. Savasta, and F. Nori, Feynman-diagrams approach to the quantum Rabi model for ultrastrong cavity QED: Stimulated emission and reabsorption of virtual particles dressing a physical excitation, *New J. Phys.* **19**, 053010 (2017).
- [67] O. Di Stefano, A. F. Kockum, A. Ridolfo, S. Savasta, and F. Nori, Photodetection probability in quantum systems with arbitrarily strong light-matter interaction, *Sci. Rep.* **8**, 17825 (2018).
- [68] A. Le Boité, Theoretical methods for ultrastrong light-matter interactions, *Adv. Quantum Technol.* **3**, 1900140 (2020).
- [69] S. Savasta, O. Di Stefano, and F. Nori, Thomas–Reiche–Kuhn (TRK) sum rule for interacting photons, *Nanophotonics* **10**, 465 (2021).
- [70] C. Gardiner and P. Zoller, *Quantum Noise* (Springer, 2004), Vol. 56.
- [71] A. Ridolfo, M. Leib, S. Savasta, and M. J. Hartmann, Photon Blockade in the Ultrastrong Coupling Regime, *Phys. Rev. Lett.* **109**, 193602 (2012).
- [72] L. Garziano, A. Ridolfo, R. Stassi, O. Di Stefano, and S. Savasta, Switching on and off of ultrastrong light-matter interaction: Photon statistics of quantum vacuum radiation, *Phys. Rev. A* **88**, 063829 (2013).
- [73] S. Franke, S. Hughes, M. K. Dezfooli, P. T. Kristensen, K. Busch, A. Knorr, and M. Richter, Quantization of Quasinormal Modes for Open Cavities and Plasmonic Cavity Quantum Electrodynamics, *Phys. Rev. Lett.* **122**, 213901 (2019).
- [74] S. Hughes, S. Franke, C. Gustin, M. K. Dezfooli, A. Knorr, and M. Richter, Theory and limits of on-demand single-photon sources using plasmonic resonators: A quantized quasinormal mode approach, *ACS Photonics* **6**, 2168 (2019).
- [75] S. Franke, M. Richter, J. Ren, A. Knorr, and S. Hughes, Quantized quasinormal-mode description of nonlinear cavity-QED effects from coupled resonators with a Fano-like resonance, *Phys. Rev. Research* **2**, 033456 (2020).
- [76] J. J. Sanchez-Mondragon, N. B. Narozhny, and J. H. Eberly, Theory of Spontaneous-Emission Line Shape in an Ideal Cavity, *Phys. Rev. Lett.* **51**, 550 (1983).
- [77] E. del Valle, F. P. Laussy, and C. Tejedor, Luminescence spectra of quantum dots in microcavities. II. Fermions, *Phys. Rev. B* **79**, 235326 (2009).
- [78] C. Cohen-Tannoudji, J. Dupont-Roc, and G. Grynberg, *Photons and Atoms-Introduction to Quantum Electrodynamics* (Wiley-VCH, 1997).

- [79] M. Wubs, L. G. Suttorp, and A. Lagendijk, Multiple-scattering approach to interatomic interactions and superradiance in inhomogeneous dielectrics, *Phys. Rev. A* **70**, 053823 (2004).
- [80] M. Babiker and R. Loudon, Derivation of the Power-Zienau-Woolley Hamiltonian in Quantum Electrodynamics by Gauge Transformation, *Proc. R. Soc. A* **385**, 439 (1983).
- [81] L. Mandel and E. Wolf, *Optical Coherence and Quantum Optics* (Cambridge University Press, 1995).
- [82] J. R. Johansson, P. D. Nation, and F. Nori, QuTiP: An open-source Python framework for the dynamics of open quantum systems, *Comput. Phys. Commun.* **183**, 1760 (2012).
- [83] J. R. Johansson, P. D. Nation, and F. Nori, QuTiP 2: A Python framework for the dynamics of open quantum systems, *Comput. Phys. Commun.* **184**, 1234 (2013).
- [84] S. Gambino, M. Mazzeo, A. Genco, O. Di Stefano, S. Savasta, S. Patane, D. Ballarini, F. Mangione, G. Lerario, D. Sanvitto, and G. Gigli, Exploring light-matter interaction phenomena under ultrastrong coupling regime, *ACS Photonics* **1**, 1042 (2014).
- [85] T. Niemczyk, F. Deppe, H. Huebl, E. Menzel, F. Hocke, M. Schwarz, J. García-Ripoll, D. Zueco, T. Hümmer, E. Solano, A. Marx, and R. Gross, Circuit quantum electrodynamics in the ultrastrong-coupling regime, *Nat. Phys.* **6**, 772 (2010).
- [86] H. Carmichael and D. Walls, Master equation for strongly interacting systems, *J. Phys. A: Math., Nucl. Gen.* **6**, 1552 (1973).